

RESEARCH ARTICLE | APRIL 03 2024

Alkali hydroxide (LiOH, NaOH, KOH) in water: Structural and vibrational properties, including neutron scattering results

Ruru Ma ; Nitish Baradwaj ; Ken-ichi Nomura ; Aravind Krishnamoorthy ; Rajiv K. Kalia ; Aiichiro Nakano ; Priya Vashishta 



J. Chem. Phys. 160, 134309 (2024)

<https://doi.org/10.1063/5.0186058>

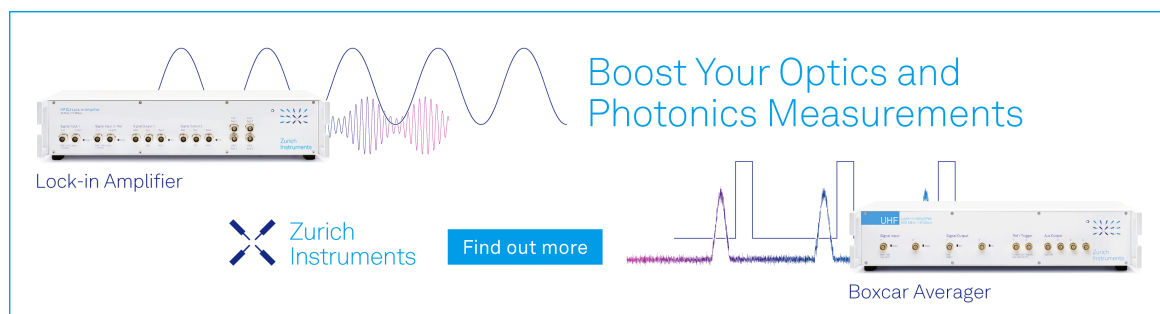


View
Online



Export
Citation

10 May 2024 16:40:05



Boost Your Optics and Photonics Measurements

Lock-in Amplifier

Zurich Instruments

Find out more

Boxcar Averager

Alkali hydroxide (LiOH, NaOH, KOH) in water: Structural and vibrational properties, including neutron scattering results

Cite as: J. Chem. Phys. 160, 134309 (2024); doi: 10.1063/5.0186058

Submitted: 3 November 2023 • Accepted: 18 March 2024 •

Published Online: 3 April 2024



View Online



Export Citation



CrossMark

Ruru Ma,¹  Nitish Baradwaj,¹  Ken-ichi Nomura,¹  Aravind Krishnamoorthy,²  Rajiv K. Kalia,¹ 
Aiichiro Nakano,¹  and Priya Vashishta^{1,a)} 

AFFILIATIONS

¹Collaboratory for Advanced Computing and Simulations, University of Southern California, Los Angeles, California 90007-0242, USA

²Department of Mechanical Engineering, Texas A & M University, College Station, Texas 77843-3123, USA

^{a)}Author to whom correspondence should be addressed: priyav@usc.edu

ABSTRACT

Structural and vibrational properties of aqueous solutions of alkali hydroxides (LiOH, NaOH, and KOH) are computed using quantum molecular dynamics simulations for solute concentrations ranging between 1 and 10M. Element-resolved partial radial distribution functions, neutron and x-ray structure factors, and angular distribution functions are computed for the three hydroxide solutions as a function of concentration. The vibrational spectra and frequency-dependent conductivity are computed from the Fourier transforms of velocity autocorrelation and current autocorrelation functions. Our results for the structure are validated with the available neutron data for 17M concentration of NaOH in water [Semrouni *et al.*, Phys. Chem. Chem. Phys. 21, 6828 (2019)]. We found that the larger ionic radius [$r(\text{Li}^+) < r(\text{Na}^+) < r(\text{K}^+)$] and higher concentration disturb the hydrogen-bond network of water, resulting in more disordered cationic hydration shell. Our *ab initio* simulation data for solute concentrations ranging between 1 and 10M can be used to guide future elastic and inelastic neutron-scattering experiments.

© 2024 Author(s). All article content, except where otherwise noted, is licensed under a Creative Commons Attribution (CC BY) license (<http://creativecommons.org/licenses/by/4.0/>). <https://doi.org/10.1063/5.0186058>

I. INTRODUCTION

Aqueous solution of alkali hydroxides (e.g., LiOH, NaOH, and KOH) are important basic solutions that are widely used in industry, for metal production,² semiconductor manufacturing,³ and batteries.⁴ Alkali metal hydroxide coatings have been known to increase the reactivity of metallic surfaces in catalytic reactions.^{5,6} The solubility of alkali hydroxides in water is high with values of 12.5 g/100 ml, 100 g/100 ml, and 121.5 g/100 ml for LiOH, NaOH, and KOH, respectively, at 298 K.⁷ These high levels of solubility provide opportunities to explore ion-solvation dynamics. The study of charged species in water is essential in understanding the chemistry of acids and bases, which forms the basis of transport across fat and lipid membranes in the human body.^{8–13} Sodium and potassium ions play an important role in the exchange of nerve signals,¹⁴ forming the basis of temperature sensing, insulin release, and cardiac contraction.

Historically, lithium has been used in psychiatric medicine.¹⁵ The importance of lithium on humanity has increased due to its widespread usage in rechargeable batteries.¹⁶ Other applications of lithium include the use of its stearates in grease production.¹⁷ Owing to its weight, lithium has applications in the aero-industry as an important addition to alloys. Lithium global consumption is touted to reach 500 000 tons by 2025.¹⁸ This increased consumption may lead to a global shortage of lithium^{19,20} in the future. It, therefore, becomes essential to look at a more green and sustainable way for Li production and recovery.^{21,22} Wei *et al.*²³ have proposed a novel way of recovering Li through the conversion of lithium phosphate to LiOH. The transport of Li ions across membranes lies at the heart of this process.

The common thread to all these applications lies in understanding the transport of alkali metal ions and the modifications to the underlying structure of water due to the ions. There have been multiple experimental^{24–33} and theoretical^{34–44} studies carried out in

this regard. Most of the studies on aqueous ionic solutions^{45–52} have revealed that the presence of the alkali ion results in local breakdown of the tetrahedral water structures. Their properties are largely governed by unique structures of hydration shells around cations (e.g., Li^+ , Na^+ , K^+) and hydroxide ions (OH^-), which have been studied extensively using neutron^{25,29,30,53,54} and x-ray^{55–57} scattering experiments. In particular, Imberti *et al.* have studied the effects of solute concentrations and ionic radius [$r(\text{Li}^+) < r(\text{Na}^+) < r(\text{K}^+)$] on the structures of cationic and hydroxide hydration shells.⁵³

Neutron experiments have also been combined with molecular-dynamics (MD) simulations to elucidate atomistic structures that produce the observed scattering data. For example, MD simulations using classical,^{1,58} quantum,⁵⁶ and neural network⁵⁹ force fields have been used to study aqueous NaOH solutions. Quantum molecular dynamics (QMD) simulations have also been performed for KOH solutions³⁷ and a comparative study of NaOH and KOH solutions.³⁹ However, comprehensive QMD simulations have not been performed to compare the structures of LiOH, NaOH, and KOH and their concentration dependence. In addition to neutron scattering for structural study, dynamic structure factors measured by inelastic neutron scattering (INS) experiments provide valuable knowledge about vibrational properties. However, QMD simulations have not been used to calculate dynamic structure factors of LiOH, NaOH, and KOH and their concentration dependence.

In this paper, we perform comprehensive QMD simulations using the accurate SCAN functional^{60,61} to study structural and vibrational properties of LiOH, NaOH, and KOH at solute concentrations ranging from 1 to 10M. We carry out a comprehensive study of cation- and concentration-dependence of element-resolved partial radial distribution functions and angular distribution functions. In addition, both neutron and x-ray structure factors are computed to guide future experiments. We also compute velocity and current autocorrelation functions and corresponding vibrational spectra and frequency-dependent conductivity to be compared with inelastic neutron scattering and other optical experiments.

II. METHOD

We used the Vienna *Ab initio* Simulation Package (VASP) software⁶² to perform quantum molecular dynamics (QMD) simulations.⁶³ The electronic states are calculated using the projector augmented-wave (PAW) method⁶⁴ in the framework of density functional theory (DFT).⁶⁵ The exchange–correlation effects are incorporated using the SCAN functional.⁶⁰

We start simulations with a bulk water configuration taken from our previous study of water,⁶¹ which contains 108 H_2O molecules. To prepare an alkali hydroxide solution with a given solute concentration, we randomly choose an appropriate number of H_2O molecules and, for each molecule, replace one of its two H atoms by one cation M ($M \in \{\text{Li}, \text{Na}, \text{K}\}$). We then adjust the simulation box size to reproduce the experimental density and relax the atomic positions to achieve a local energy-minimum configuration.

After setting up the initial configuration, we first thermalize the system by performing a QMD simulation in the canonical ensemble (NVT) at temperature 303 K for 1000 steps, 0.4 ps with a time step of 0.4 fs, followed by longer NVT thermalization for 8 ps with a time

step of 1 fs. To obtain a room temperature configuration, we perform a QMD simulation in the microcanonical ensemble (NVE) for 2 ps with a time step of 0.25 fs, where the temperature controlled every 40 fs. Finally, we perform a MD simulation in the uninterrupted NVE ensemble for 5 ps with a time step of 0.25 fs to compute structural and vibrational correlation functions.

III. VALIDATION OF SIMULATION RESULTS WITH NEUTRON SCATTERING EXPERIMENTS

To validate our simulation results, we first compare calculated structural properties with a recent neutron-scattering experiment on NaOH by Semrouni *et al.*, Phys. Chem. Chem. Phys. **21**(13), 6828 (2019).¹ To accomplish this, we have applied the method described above to 17M NaOH water solution as in the neutron scattering experiment. For this system, we have computed the partial pair distribution function $g_{\alpha\beta}(r)$, total pair distribution function $g(r)$,⁶⁶ and neutron pair distribution function $g_N(r)$.⁶⁶ The neutron pair distribution function is defined as

$$g_N(r) = \frac{\sum_{\alpha,\beta} c_\alpha b_\alpha c_\beta b_\beta g_{\alpha\beta}(r)}{(\sum_\alpha b_\alpha c_\alpha)^2}, \quad (1)$$

where r is the pair distance and c_α and b_α are the concentration and coherent neutron-scattering length of species α , respectively. Figure 1 shows plots of pair distribution functions of Na–Na (magenta), Na–H (red), Na–O (blue), H–H (green), H–O (purple), and O–O (orange). The brown line shows the total pair distribution function $g(r)$. In the top figure, the blue and black lines, respectively, represent the simulation and experimental¹ data for $g_N(r)$. Our simulation results and experimental results are in good agreement, while the simulated $g_{\alpha\beta}(r)$ in Fig. 1 elucidates the origin of each peak in $g_N(r)$. Namely, the first peak at 1 Å comes from the intramolecular H–O covalent bond, while the second peak at 1.7 Å is from the hydrogen bonds H–O and H–H. The third small bump around 2.2 Å is mainly from Na–O, and Na–H also contributes to it. The fourth peak around 3 Å mainly comes from H–O, and Na–Na also contributes to it. The good agreement of the simulation data with the experiment data thus validates our simulation method for these systems.

To generate the neutron RDF $g_N(r)$, Semrouni *et al.*¹ used a Lorch modification function and a value of q_{max} of 40 Å^{−1}. In addition to this, the authors removed the incoherent scattering from the D-atom by subtracting real space intensity with a threshold value of 0.7 Å using various Fourier filter methods.^{67,68} These parameters have a small range of tolerance to produce slightly different neutron RDF plots. Our results from QMD mostly agree with their experimental results. However, it is likely that small differences between QMD simulations and experimentally derived $g(r)$, in 2–4 Å range, could be reduced a bit from slightly different choices of values for these filter parameters. It should be noted, however, that minor discrepancies between experimental and QMD simulations are to be expected because of the approximate exchange–correlation functional used in DFT for implementing QMD simulations. In addition, these discrepancies can be used as a guide to refine the exchange–correlation functional in DFT for this class of systems.^{69,70}

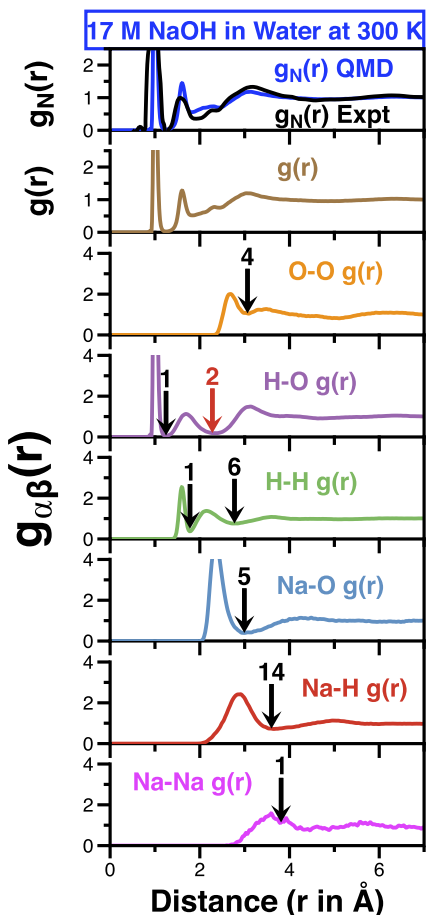


FIG. 1. Partial pair distribution function $g_{\alpha\beta}(r)$, total pair distribution function $g(r)$, and neutron pair distribution function $g_N(r)$ of 17M NaOH in water solution at 300 K. Na–Na pair, magenta; Na–H pair, red; Na–O pair, blue; H–H pair, green; H–O pair, purple; O–O pair, orange; $g(r)$, brown; $g_N(r)$, blue. The black line is experimental $g_N(r)$ from reference. Numerals are coordination numbers at distances marked by the black arrows. In the fourth figure from the top, the red arrow with a coordination of 2 indicates the hydrogen bond.

To provide more complete reference data for recent and future scattering experiments, we also compute partial static structure factors from the Fourier transform of corresponding partial pair distribution functions,⁶⁶

$$S_{\alpha\beta}(q) = \delta_{\alpha\beta} + 4\pi\rho(c_\alpha c_\beta)^{1/2} \int_0^\infty [g_{\alpha\beta}(r) - 1] \frac{\sin(qr)}{qr} r^2 dr, \quad (2)$$

where q is the wave number, ρ is the total number density, and c_α is the concentration of species α .

The neutron-scattering static structure is obtained from the partial static structure factors by weighting them with concentration and coherent neutron-scattering lengths,⁶⁶

$$S_N(q) = \frac{\sum_{\alpha,\beta} b_\alpha b_\beta (c_\alpha c_\beta)^{1/2} S_{\alpha\beta}(q) [S_{\alpha\beta}(q) - \delta_{\alpha\beta} + (c_\alpha c_\beta)^{1/2}]}{(\sum_\alpha b_\alpha c_\alpha)^2}, \quad (3)$$

where b_α is the coherent neutron-scattering length of species α .

The x-ray structure factor is obtained by⁶⁶

$$S_X(q) = \frac{\sum_{\alpha,\beta} f_\alpha f_\beta (c_\alpha c_\beta)^{1/2} S_{\alpha\beta}(q)}{(\sum_\alpha f_\alpha c_\alpha)^2}, \quad (4)$$

where f_α is the x ray form factor of species α .

Figure 2 shows $S_{\alpha\beta}(q)$ for Na–Na (magenta), Na–H (red), Na–O (blue), H–H (green), H–O (purple), and O–O (orange) pairs; $S_N(q)$ (brown); and $S_X(q)$ (blueberry).

The DFT based first-principles simulation, where the atoms are treated classically and the electron charge density is treated quantum-mechanically to compute atomic forces, can lead to discrepancies with experimental data, when we are dealing with hydrogen motion at low temperatures. The nuclear quantum effect (NQE) induced anharmonicity is expected to be quite common in molecular solids/liquids at low temperatures, especially in systems with “flexible” groups such as –OH, –CH₃, and –NH₂.

A promising solution is path integral molecular dynamics (PIMD), in which the quantum partition function is mapped to a

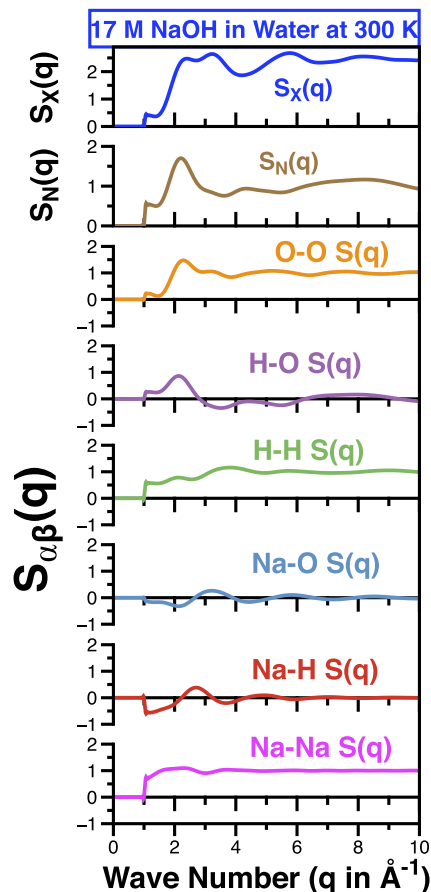


FIG. 2. Partial structure factor $S_{\alpha\beta}(q)$, neutron structure factor $S_N(q)$, and x-ray structure factor $S_X(q)$ of 17M NaOH in water solution at 300 K. Na–Na pair, magenta; Na–H pair, red; Na–O pair, blue; H–H pair, green; H–O pair, purple; O–O pair, orange; $S_N(q)$, brown; $S_X(q)$, blueberry.

classical analog by using replicas (beads) connected by springs (ring polymers) to represent each atom,^{71–73} which effectively extends the phase space of the atomic system due to their zero-point motion. This method is suited for problems when the particle zero-point energy is not negligible with respect to the average thermal energy, which is expected for hydrogen systems at low temperatures, such as water and ammonia. We have examined the dynamics of ammonia in liquid phase through PIMD simulations of 864 NH₃ molecules in a cubic simulation box of side 32 Å at 205 K.⁷⁴

As most of the computational expense for *ab initio* PIMD simulations comes from having to compute multiple replica DFT simulations, the computational cost can be significantly decreased if the underlying DFT simulations can be replaced by much cheaper computational models. To accomplish this, we perform neural network quantum molecular dynamics (NNQMD) based PIMD simulations utilizing the recently developed group-theoretically equivariant neural-network force field model called Allegro.⁷⁵

In our inelastic neutron scattering (INS) study of solid and liquid ammonia, we compared the INS measurements to DFT simulations.⁷⁴ We find that NQE induced anharmonicity fundamentally changes the predicted spectrum with conventional DFT simulations, where we use neural network based PIMD simulations. PIMD simulations can reproduce the hardening of N–H stretching modes in the liquid phase.

In our simulations of water–alkali hydride solutions at room temperature, the effect of NQE of hydrogen is expected to be rather

small. Besides this, there are still uncertainties in as-practiced DFT computations, where pseudo-potential approximation and exchange–correlation approximations are used. There are varying degrees of small errors in structural properties due to these two approximations and more serious discrepancies in dynamical behavior. However, it should be said that DFT based simulations do provide a semi-quantitative description of structural properties of materials.

IV. RESULTS

Having validated the simulation method for NaOH for 17M concentration, we now present comprehensive structural and vibrational properties for aqueous solutions of alkali hydroxides (LiOH, NaOH, and KOH) using the same QMD method for solute concentrations ranging between 1 and 10M.

A. Structural properties

To study structural properties, we first calculate the partial pair distribution function, $g_{\alpha\beta}(r)$.⁶⁶ Figures 3–6 plot the M–M (magenta), M–H (red), M–O (blue), H–H (green), H–O (purple), and O–O (orange) pair distribution functions for MOH (M ∈ {Li, Na, K}), respectively, for 1, 2, 4, and 10M solute concentrations. For comparison and guidance, H–H, H–O, and O–O pair distribution functions of pure water are shown as black dashed

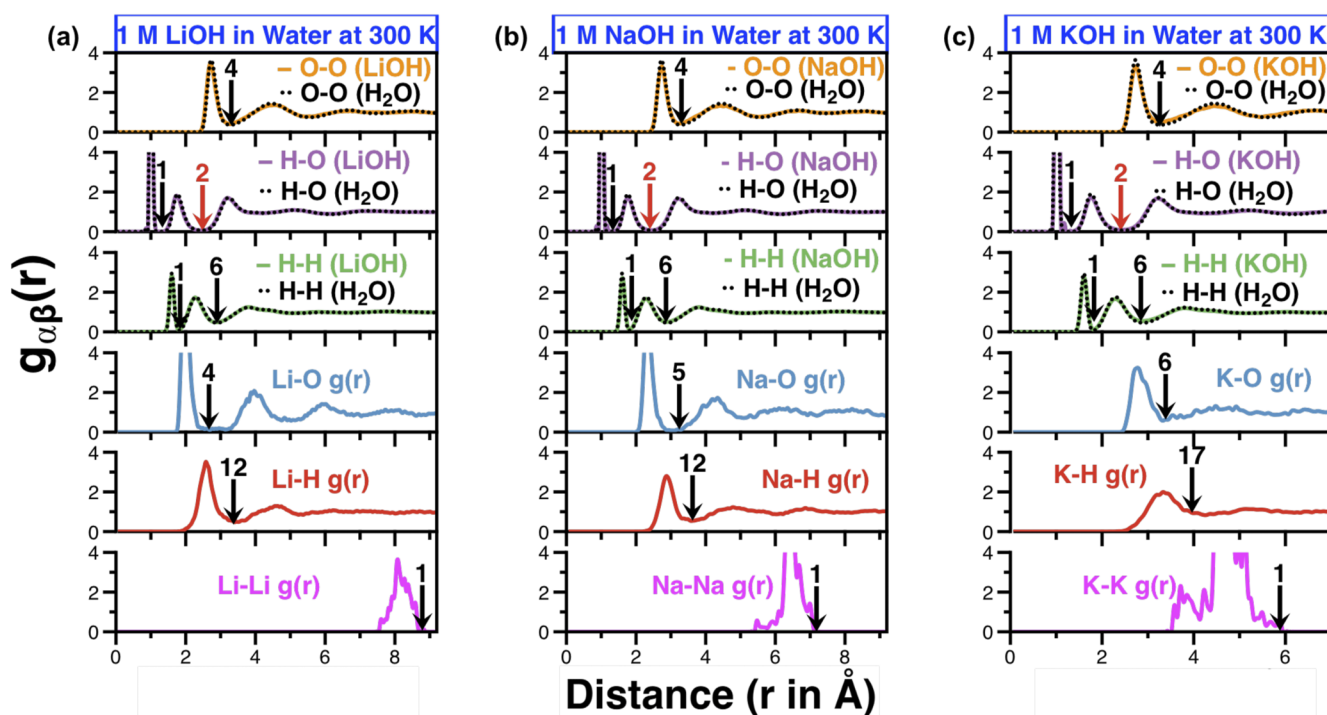


FIG. 3. Partial pair distribution function of 1M LiOH (a), NaOH (b), and KOH (c) in water solution at 300 K. The solid lines are for MOH solution (M = Li, Na, K), and the dotted lines are for pure water. M–M pair, magenta; M–H pair, red; M–O pair, blue; H–H pair, green; H–O pair, purple; O–O pair, orange. The coordination numbers are marked by black arrows. In the second figure from the top, the red arrow with coordination of 2 indicates the hydrogen bond.

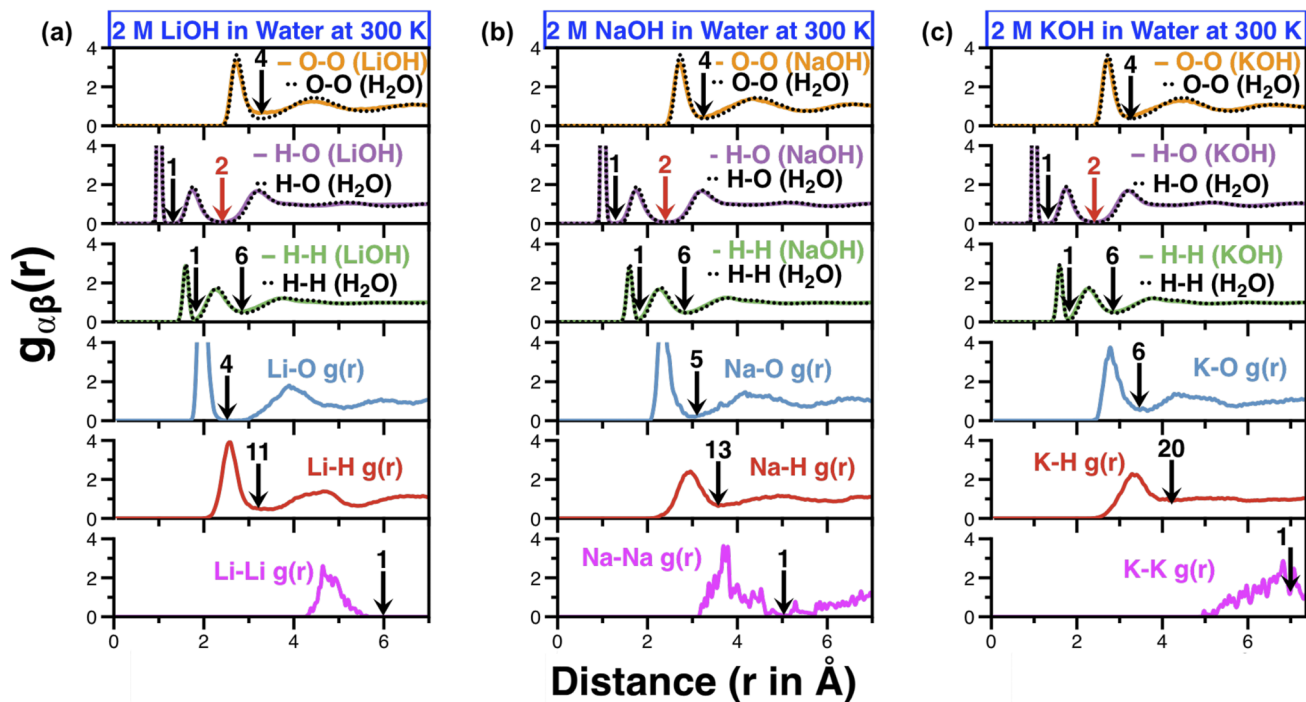


FIG. 4. Partial pair distribution function of 2M LiOH (a), NaOH (b), and KOH (c) in water solution at 300 K. The solid lines are for MOH solution ($M = \text{Li, Na, K}$), and the dotted lines are for pure water. M-M pair, magenta; M-H pair, red; M-O pair, blue; H-H pair, green; H-O pair, purple; O-O pair, orange. The coordination numbers are marked by black arrows. In the second figure from the top, the red arrow with coordination of 2 indicates the hydrogen bond.

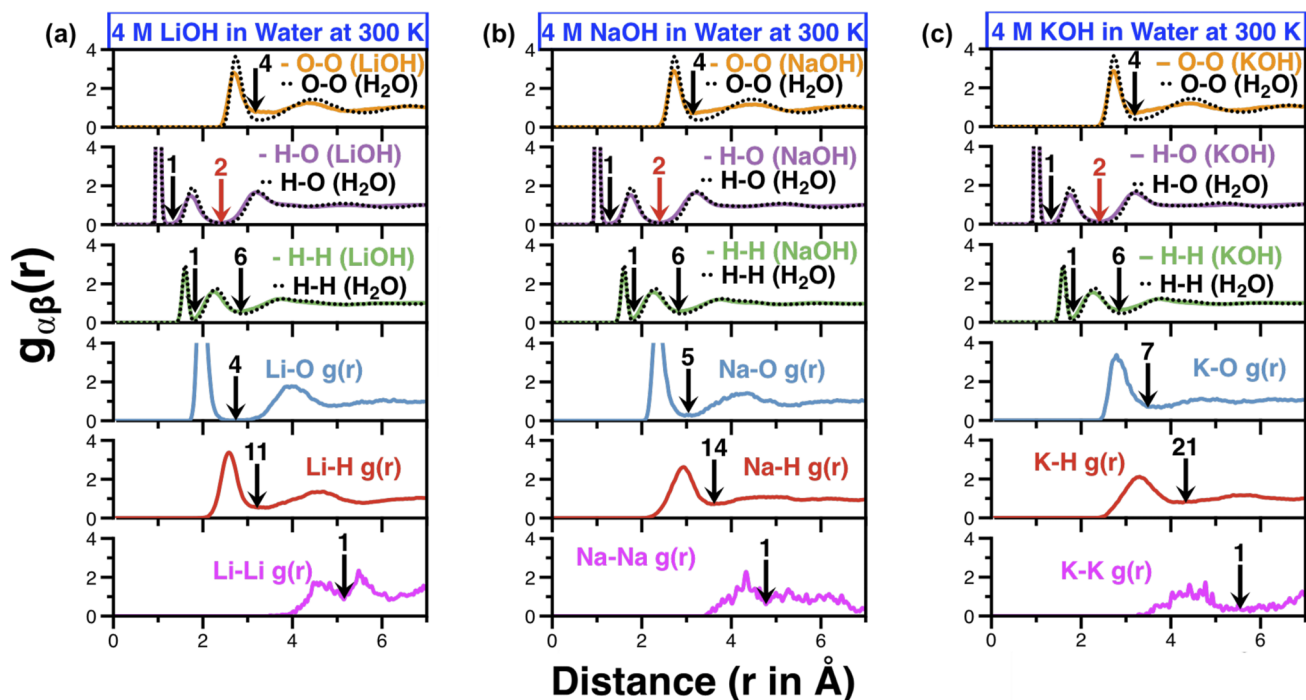


FIG. 5. Partial pair distribution function of 4M LiOH (a), NaOH (b), and KOH (c) in water solution at 300 K. The solid lines are for MOH solution ($M = \text{Li, Na, K}$), and the dotted lines are for pure water. M-M pair, magenta; M-H pair, red; M-O pair, blue; H-H pair, green; H-O pair, purple; O-O pair, orange. The coordination numbers are marked by black arrows. In the second figure from the top, the red arrow with coordination of 2 indicates the hydrogen bond.

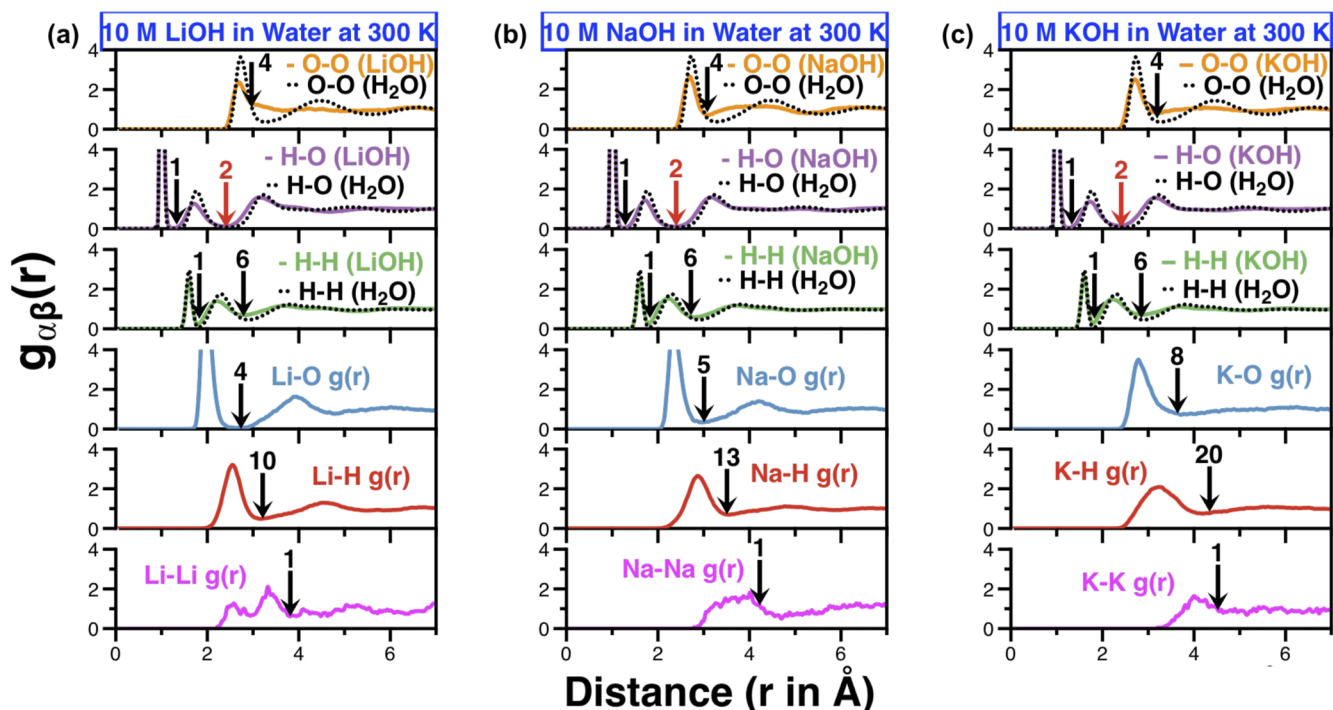


FIG. 6. Partial pair distribution function of 10M LiOH (a), NaOH (b), and KOH (c) in water solution at 300 K. The solid lines are for MOH solution ($M = \text{Li, Na, K}$), and the dotted lines are for pure water. M–M pair, magenta; M–H pair, red; M–O pair, blue; H–H pair, green; H–O pair, purple; O–O pair, orange. The coordination numbers are marked by black arrows. In the second figure from the top, the red arrow with coordination of 2 indicates the hydrogen bond.

lines. Each black arrow is labeled by the coordination number at that position. For each red arrow for $g_{\text{HO}}(r)$, the coordination number includes a hydrogen bond.

To highlight the concentration dependence of the structural correlations, Fig. 7 compares the total pair distribution function $g(r)$ ⁶⁶ of MOH ($M \in \{\text{Li, Na, K}\}$) with 1, 2, 4, and 10M concentrations. The blue, green, purple, and orange lines correspond to 1, 2, 4, and 10M.

In Fig. 8, we show the neutron pair distribution function $g_{\text{N}}(r)$ of MOD ($M \in \{\text{Li, Na, K}\}$) with 1, 2, 4, and 10M solute concentrations. The blue, green, purple, and orange lines correspond to 1, 2, 4, and 10M.

From Figs. 3–6 for $g_{\alpha\beta}(r)$ for the four molar concentrations of LiOH, NaOH, and KOH along with $g(r)$ and $g_{\text{N}}(r)$ in Figs. 7 and 8, we infer the following. The first peak in $g(r)$ and $g_{\text{N}}(r)$ at 1 Å is entirely from the O–H covalent bond. The second peak around 1.8 Å is from the O···H hydrogen bond, and its height is affected by the concentration of $M = \text{Li, Na, and K}$. From the second peak in H–H $g_{\alpha\beta}(r)$ in Figs. 3–6, it is clear that the height of this peak is consistently lower than that in pure water, as we should expect. However, this O···H hydrogen bond peak overlaps with the H–H peak that arises from water molecules also at 1.8 Å. The sum of these two main contributions is reflected in the second peak in $g(r)$ and $g_{\text{N}}(r)$ in Figs. 7 and 8. The region between 2.2 and 3 Å reflects direct contributions from Li–O, Na–O, and K–O bonds. From Figs. 3–6, one can see that, at all concentrations, the M–O

peak shifts to larger distances due to a larger size of $\text{K} > \text{Na} > \text{Li}$. The Li–O peak is at 2 Å, the Na–O peak is at 2.3 Å, and the K–O peak is at 2.8 Å. This is clearly the size effect of the three ions. The other prominent peak that overlaps in this region is the H···O–H peak at 2.2 Å. A monotonic behavior in the height of the second peak in $g(r)$ and $g_{\text{N}}(r)$ due to the hydrogen bond H···O is only seen for LiOH in water; see Table I. This is mainly because Li is a small ion and does not cause major disturbances in the hydrogen bond network. In summary, the region between 2.2 and 3 Å in $g(r)$ and $g_{\text{N}}(r)$ reflects the contributions from the M–O and M–H peaks as well as the hydrogen bond H···O–H seen as the second peak in H–H $g_{\alpha\beta}(r)$.

In Table I, we can clearly see the ion size effect $\text{K} > \text{Na} > \text{Li}$. Li disturbs the hydrogen bond network, the least and the second peak height is monotonically decreasing with concentration for the LiOH system, whereas the larger size effect of Na and K combined with increasing concentration kills this simple pattern.

In Figs. 9–12, we show $S_{\alpha\beta}(q)$ for M–M (magenta), M–H (red), M–O (blue), H–H (green), H–O (purple), and O–O (orange) pairs for MOH ($M \in \{\text{Li, Na, K}\}$), respectively, for 1, 2, 4, and 10M solute concentrations.

Figure 13 shows the neutron structure factor of deuterated MOD ($M \in \{\text{Li, Na, K}\}$) at 1, 2, 4, and 10M solute concentrations. The blue, green, purple, and orange lines correspond to 1, 2, 4, and 10M. The radius where the highest peak occurs is increasing with higher concentration.

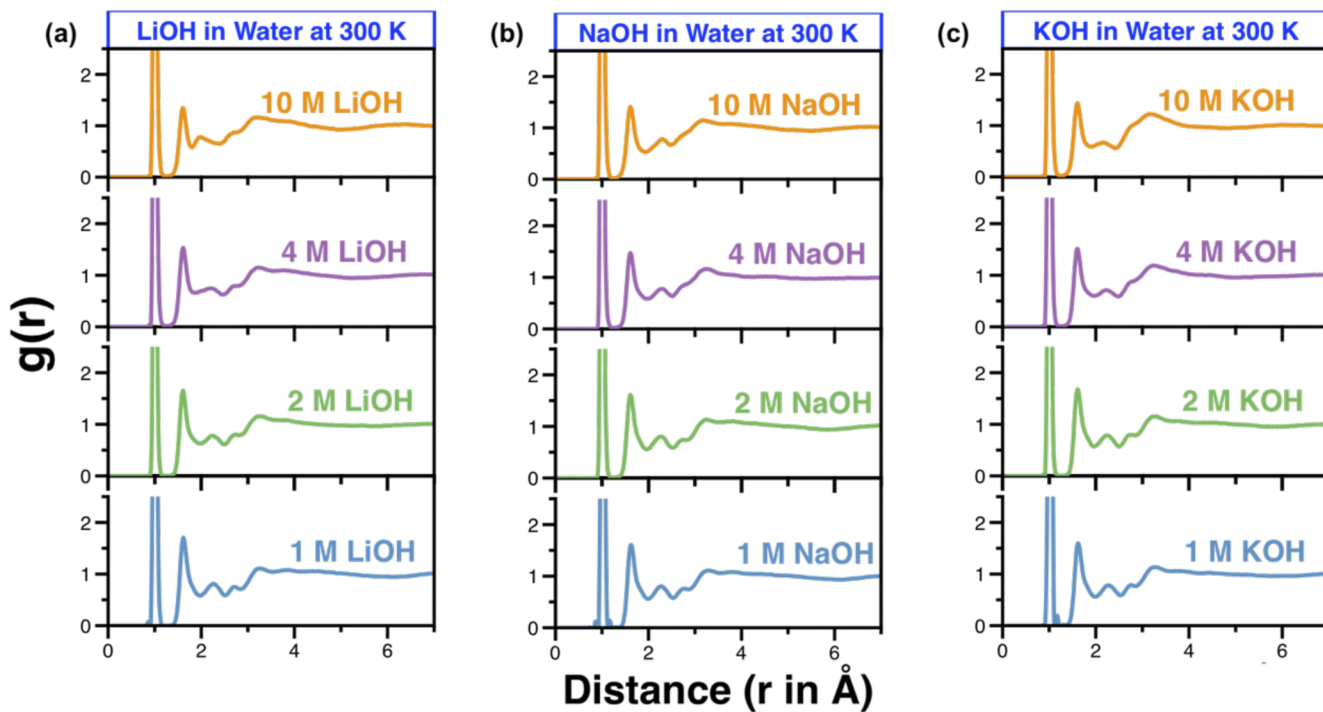


FIG. 7. Total pair distribution function of LiOH (a), NaOH (b), and KOH (c) in water solution at 300 K. 1M MOH, blue; 2M MOH, green; 4M MOH, purple; 10M MOH, orange. M = Li, Na, K.

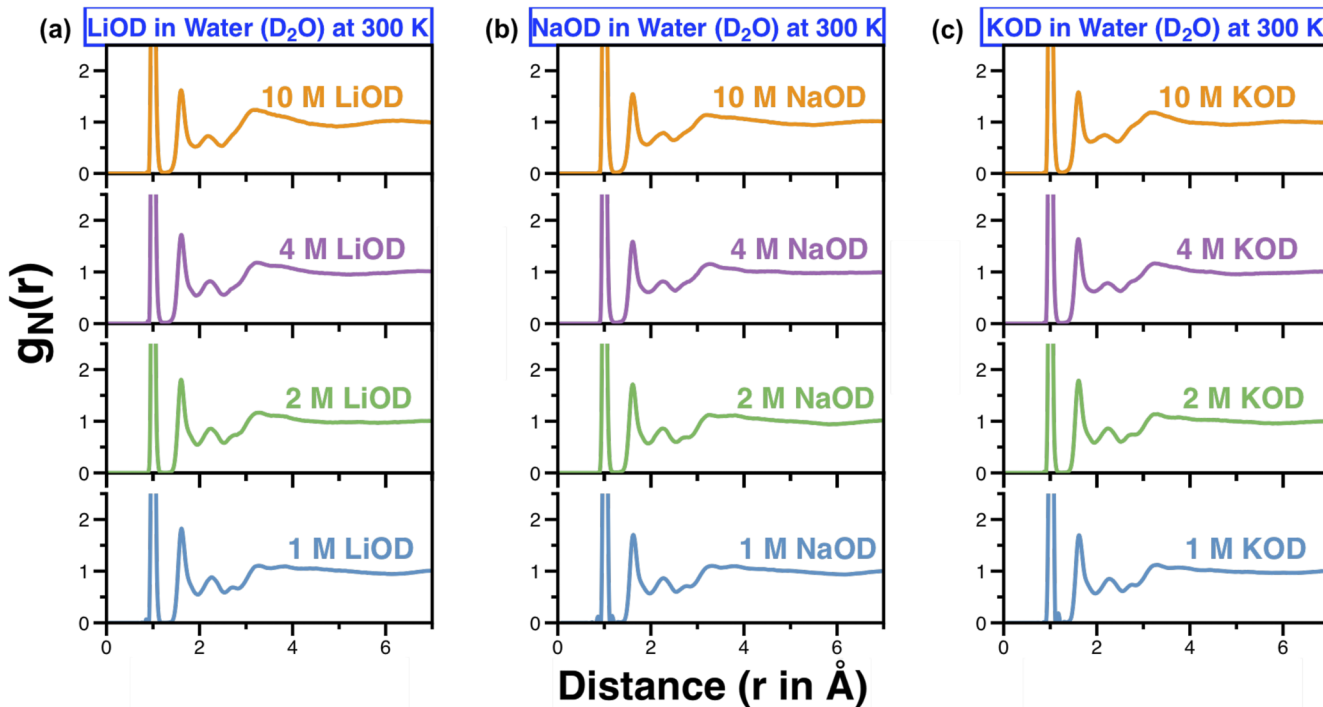


FIG. 8. Neutron pair distribution function of LiOD (a), NaOD (b), and KOD (c) in water (D_2O) solution at 300 K. 1M MOD, blue; 2M MOD, green; 4M MOD, purple; 10M MOD, orange. M = Li, Na, K.

TABLE I. Second peak height of $g(r)$ and $g_N(r)$ from Figs. 7 and 8. Li, green; Na, blue; K, red.

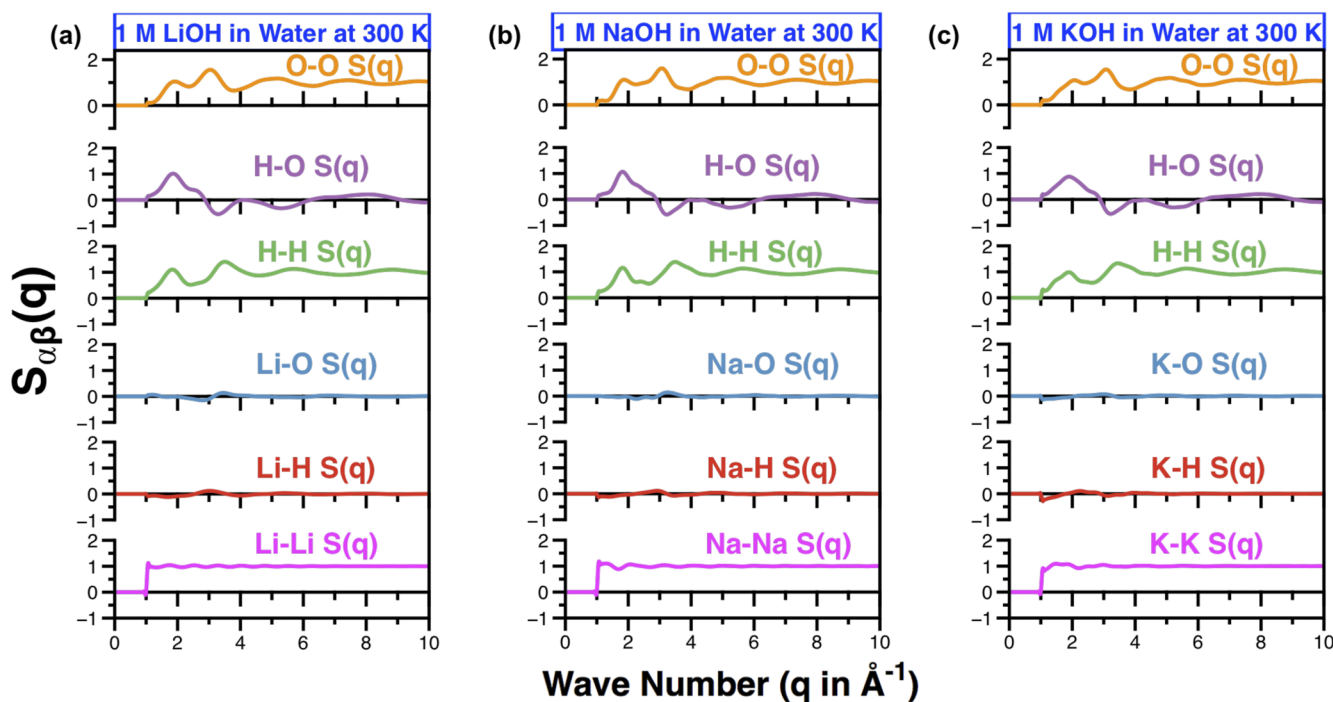
Li/K/Na Molarity (M)	$g(r)$ second peak height	$g_N(r)$ second peak height
1	1.70	1.82
2	1.65	1.80
4	1.51	1.69
10	1.31	1.59
1	1.53	1.60
2	1.60	1.70
4	1.44	1.55
10	1.50	1.54
1	1.52	1.63
2	1.67	1.77
4	1.50	1.61
10	1.42	1.60

Figure 14 shows the x-ray structure factor of MOH ($M \in \{\text{Li, Na, K}\}$) at 1, 2, 4, and 10M solute concentrations. The blue, green, purple, and orange lines correspond to 1, 2, 4, and 10M.

To study further details of the structural correlations, Figs. 15–18 show bond-angle distributions,⁶⁶ respectively, at concentrations 1, 2, 4, and 10M. The black dashed lines represent the angles \sphericalangle H–O–H and \sphericalangle O–O–O for pure water. One notable

observation is the large concentration dependence of the O–O–O distribution. At the lowest concentration of 1M (Fig. 15), the O–O–O distribution is close to that of pure water (black dotted line), where the distributions of LiOH and water are nearly identical, indicating little effect of solute on the hydrogen-bond (HB) network in water. Meanwhile, we observe slightly more deviation from the water case in NaOH and KOH. This is likely due to the larger ionic radii of Na and K compared to that of Li, which geometrically disturb the HB network to a greater extent.

To study the effects of solute concentrations and ionic radii on the cation hydration shell, Fig. 19 compares all three cation-oxygen coordination numbers $n_{\text{MO}}(r)$ ($M \in \{\text{Li, Na, K}\}$) for different concentrations. The gray dashed lines signify the coordination number of 4, 5, and 6. In Fig. 19(a), for 1M, we see $n_{\text{LiO}}(r) = 4$ between 2.3 and 3.2 Å for LiOH, which indicates a clearly delineated hydration shell consisting of four oxygens. In contrast, $n_{\text{NaO}}(r)$ and $n_{\text{KO}}(r)$ do not exhibit flat $n(r)$ for any radii in the range 2.5–3.5 Å, which indicates less ordered hydration shells for NaOH and KOH. In contrast to $n_{\text{LiO}}(r)$, $n_{\text{NaO}}(r)$ and $n_{\text{KO}}(r)$ do not have a clear hydration shell that exhibits a radius range for which $n(r)$ is flat. Accordingly, we define the hydration-shell radius as an inflection point, where the $n(r)$ curve crosses over from convex to concave. In Fig. 19(a), for NaOH, the inflection point of $n_{\text{NaO}}(r)$ is ~ 3 Å, where $n_{\text{NaO}}(r)$ value is = 5. Namely, aqueous NaOH has a diffuse cation hydration shell that contains approximately five oxygens, more than four in LiOH. For $n_{\text{KO}}(r)$, the inflection point is at larger than 3 Å, where $n_{\text{KO}}(r)$ value is = 6 or larger. This signifies an even more diffuse and longer-range hydration shell containing more O atoms

**FIG. 9.** Partial structure factor of 1M LiOH (a), NaOH (b), and KOH (c) in water solution at 300 K. M–M pair, magenta; M–H pair, red; M–O pair, blue; H–H pair, green; H–O pair, purple; O–O pair, orange. M = Li, Na, K.

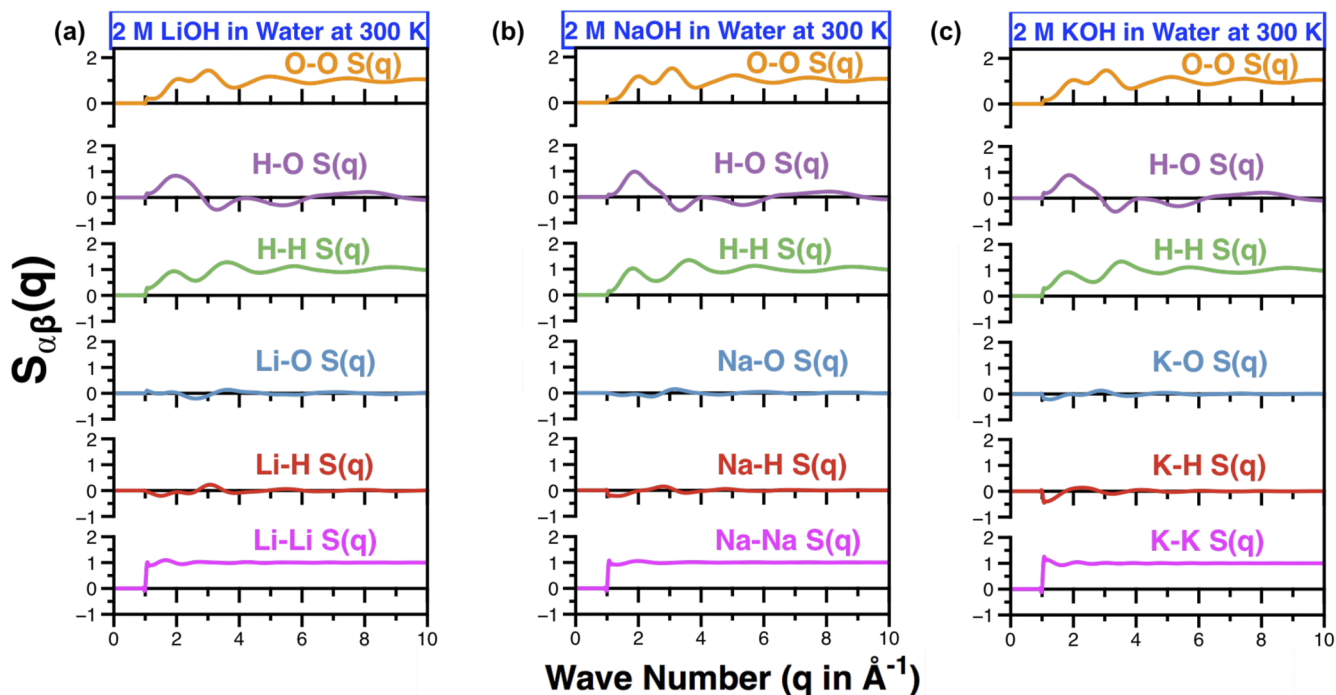


FIG. 10. Partial structure factor of 2M LiOH (a), NaOH (b), and KOH (c) in water solution at 300 K. M-M pair, magenta; M-H pair, red; M-O pair, blue; H-H pair, green; H-O pair, purple; O-O pair, orange. M = Li, Na, K.

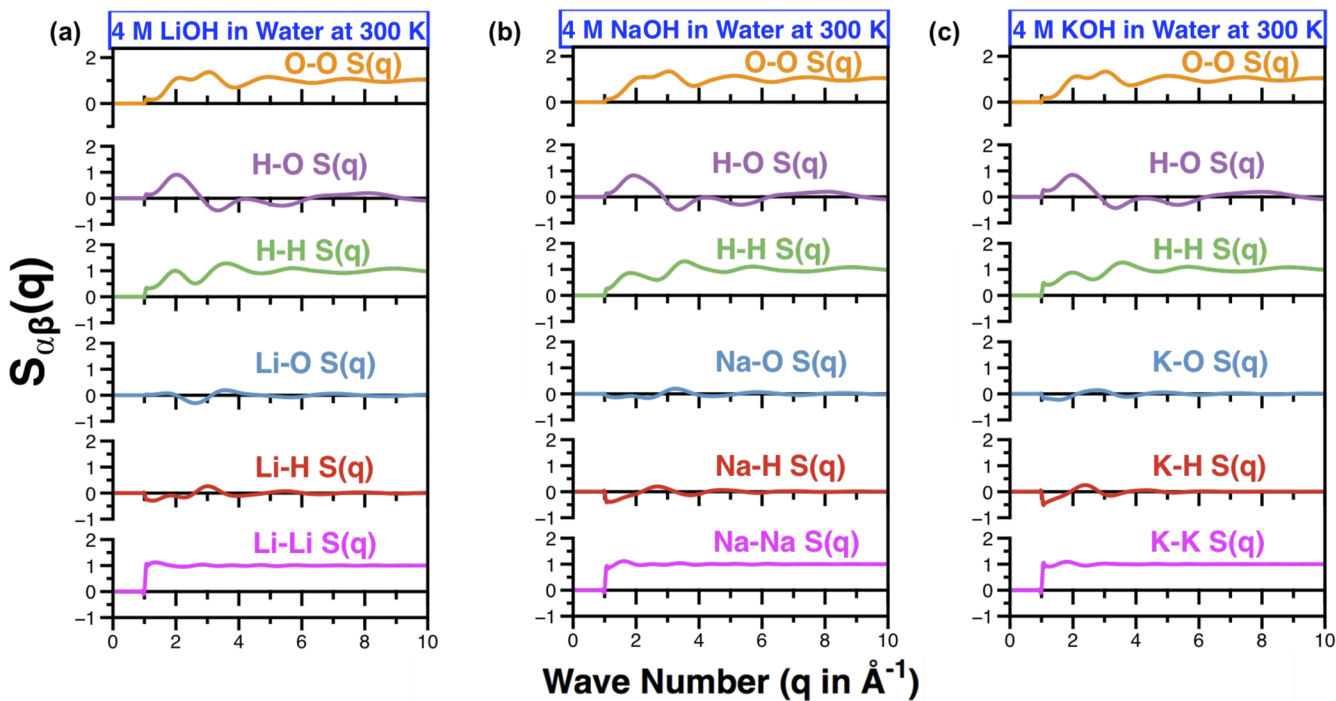


FIG. 11. Partial structure factor of 4M LiOH (a), NaOH (b), and KOH (c) in water solution at 300 K. M-M pair, magenta; M-H pair, red; M-O pair, blue; H-H pair, green; H-O pair, purple; O-O pair, orange. M = Li, Na, K.

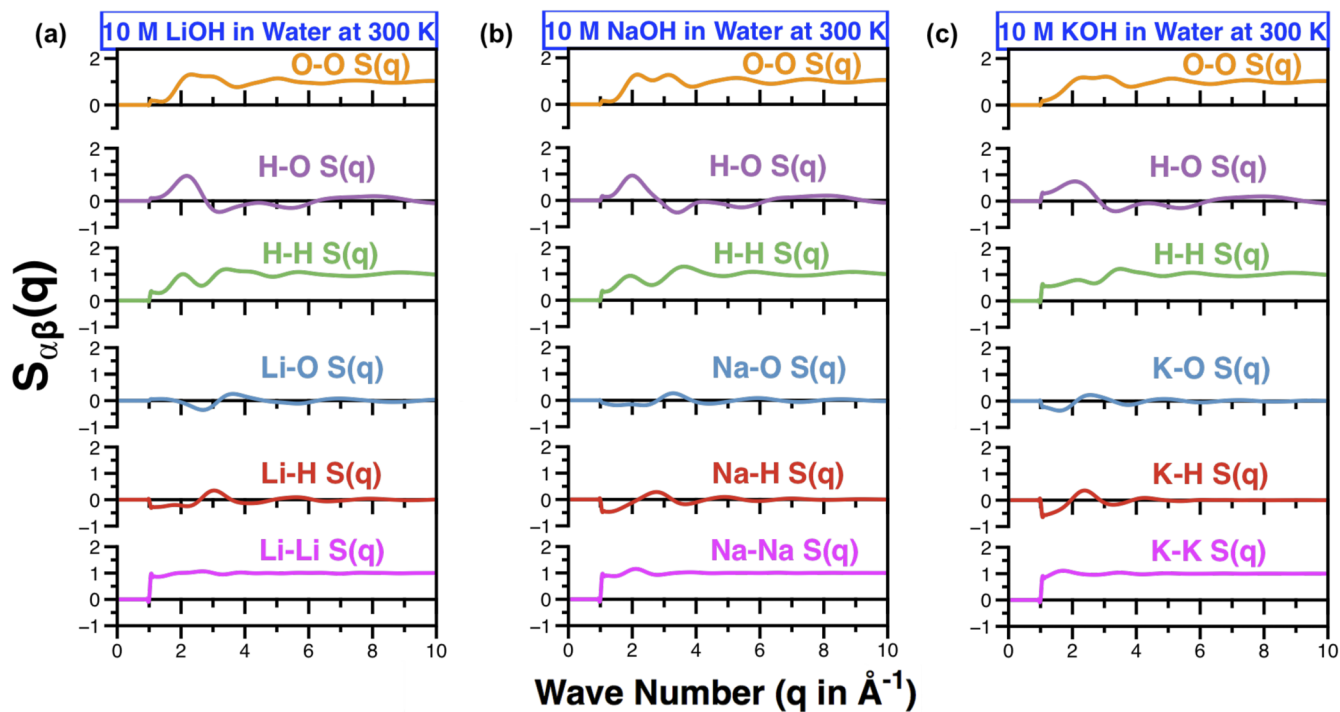


FIG. 12. Partial structure factor of 10M LiOH (a), NaOH (b), and KOH (c) in water solution at 300 K. M–M pair, magenta; M–H pair, red; M–O pair, blue; H–H pair, green; H–O pair, purple; O–O pair, orange. M = Li, Na, K.

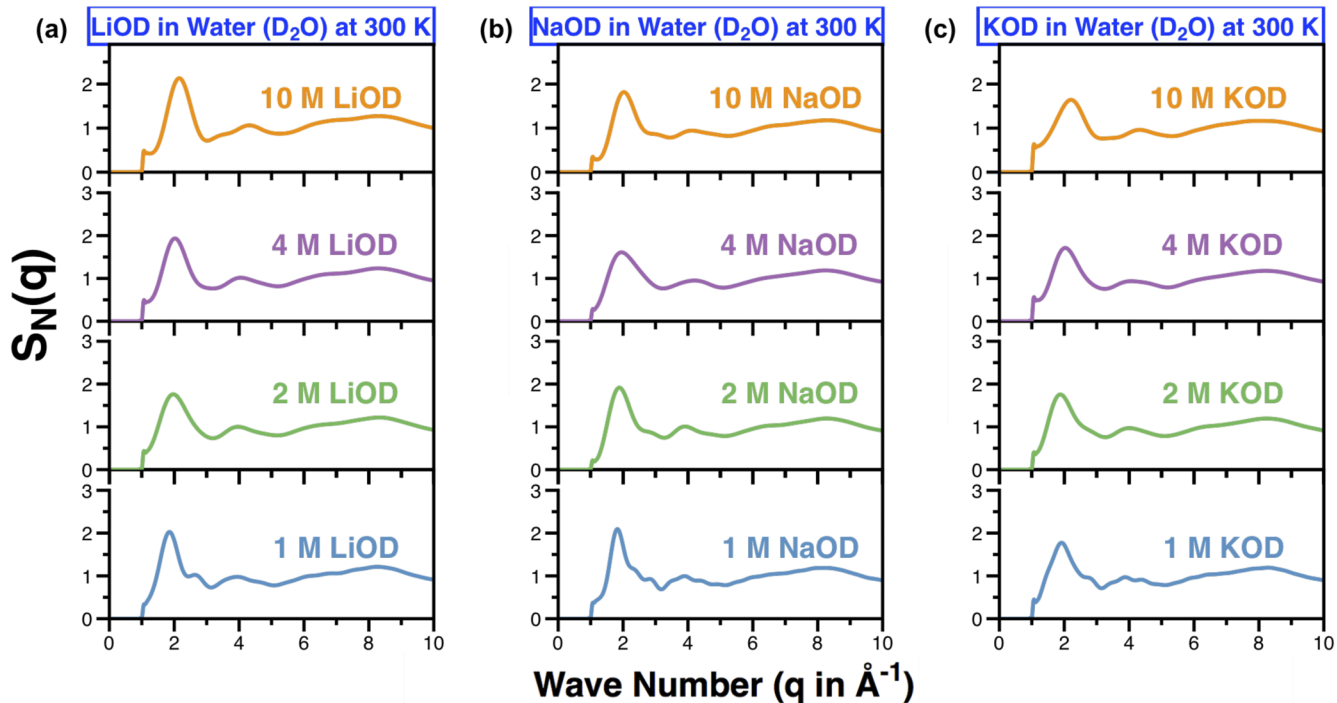


FIG. 13. Neutron structure factor of LiOD (a), NaOD (b), and KOD (c) in water (D_2O) solution at 300 K. 1M MOD, blue; 2M MOD, green; 4M MOD, purple; 10M MOD, orange. M = Li, Na, K.

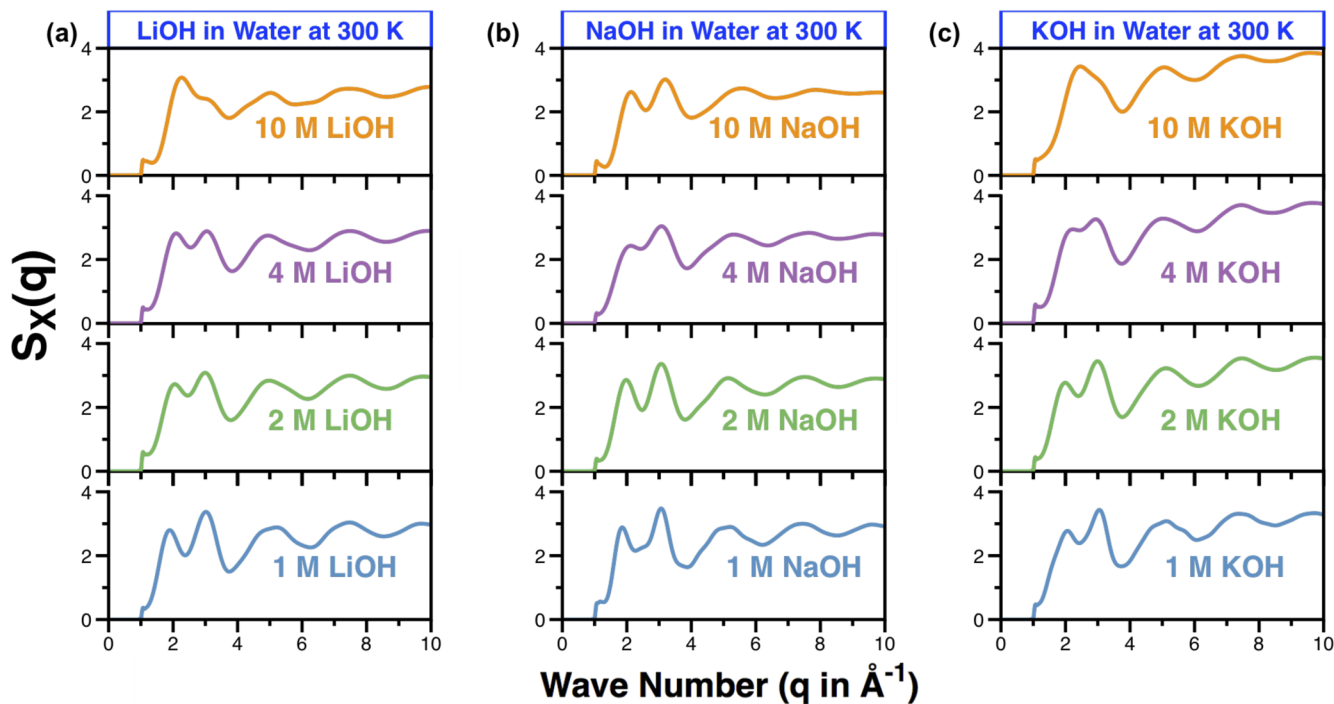


FIG. 14. X-ray structure factor of LiOH (a), NaOH (b), and KOH (c) in water solution at 300 K. 1M MOH, blue; 2M MOH, green; 4M MOH, purple; 10M MOH, orange. M = Li, Na, K.

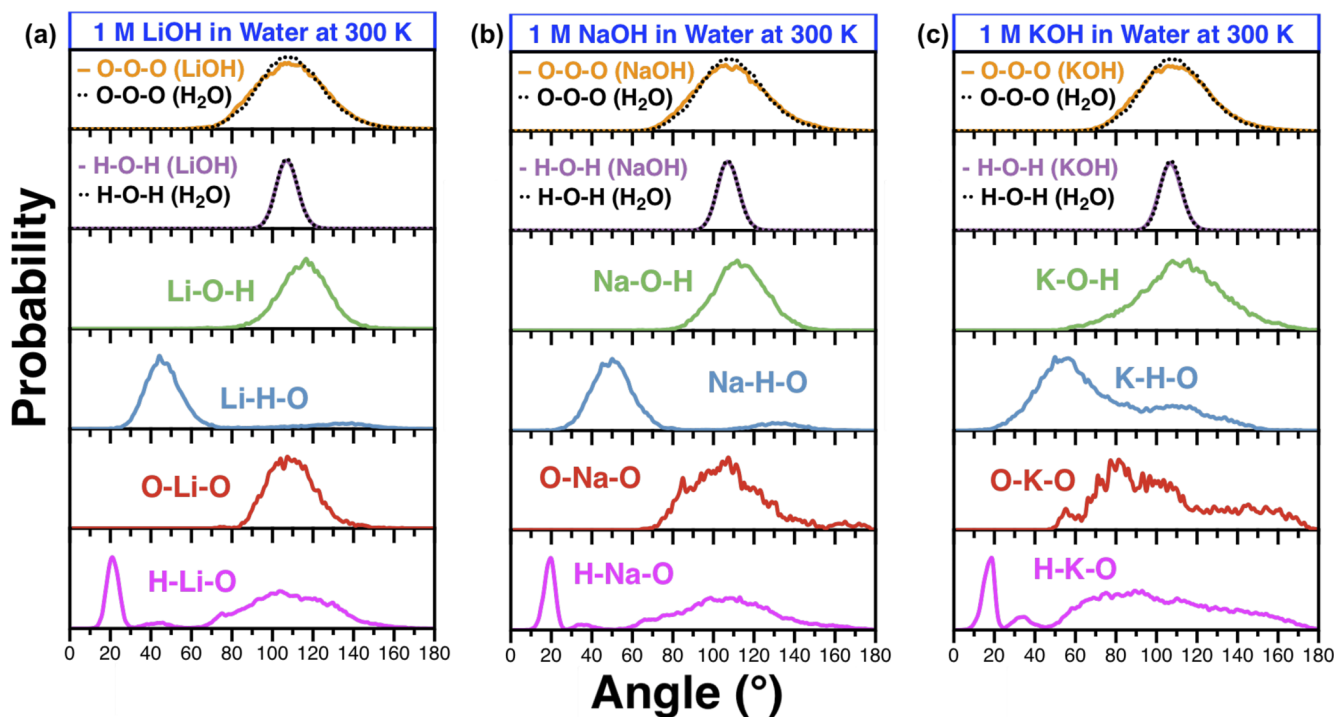


FIG. 15. Bond angle of 1M LiOH (a), NaOH (b), and KOH (c) in water solution at 300 K. The solid lines are for MOH solution (M = Li, Na, K), and the dotted lines are for pure water. H-M-O, magenta; O-M-O, red; M-H-O, blue; M-O-H, green; H-O-H, purple; O-O-O, orange. M = Li, Na, K.

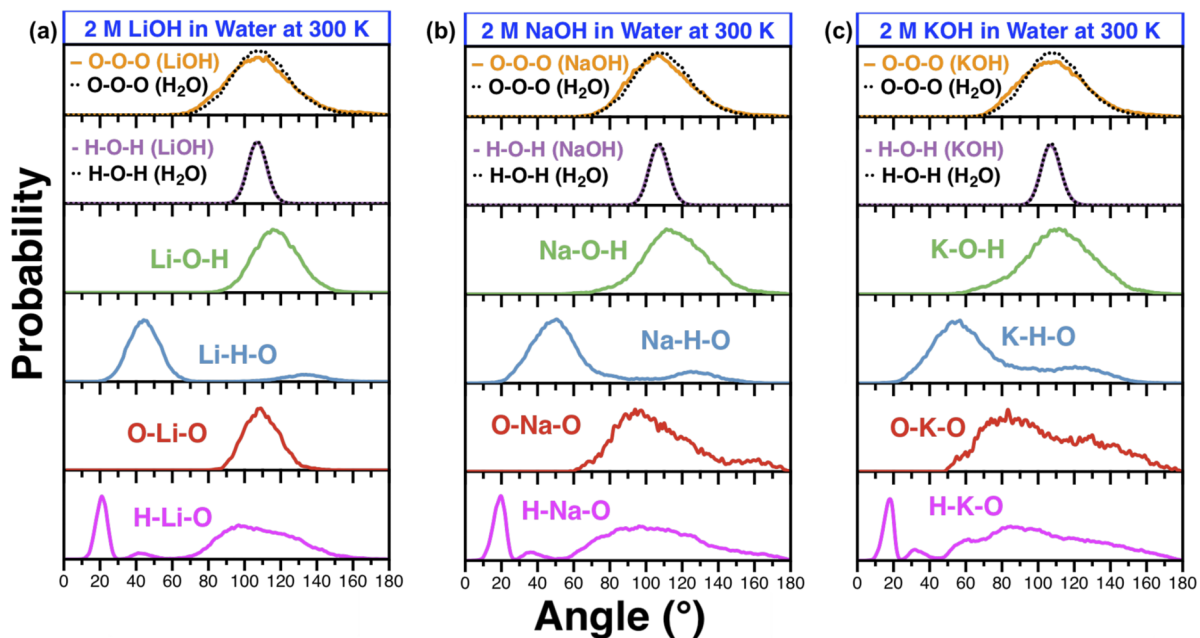


FIG. 16. Bond angle of 2M LiOH (a), NaOH (b), and KOH (c) in water solution at 300 K. The solid lines are for MOH solution ($M = \text{Li, Na, K}$), and the dotted lines are for pure water. H-M-O, magenta; O-M-O, red; M-H-O, blue; M-O-H, green; H-O-H, purple; O-O-O, orange. $M = \text{Li, Na, K}$.

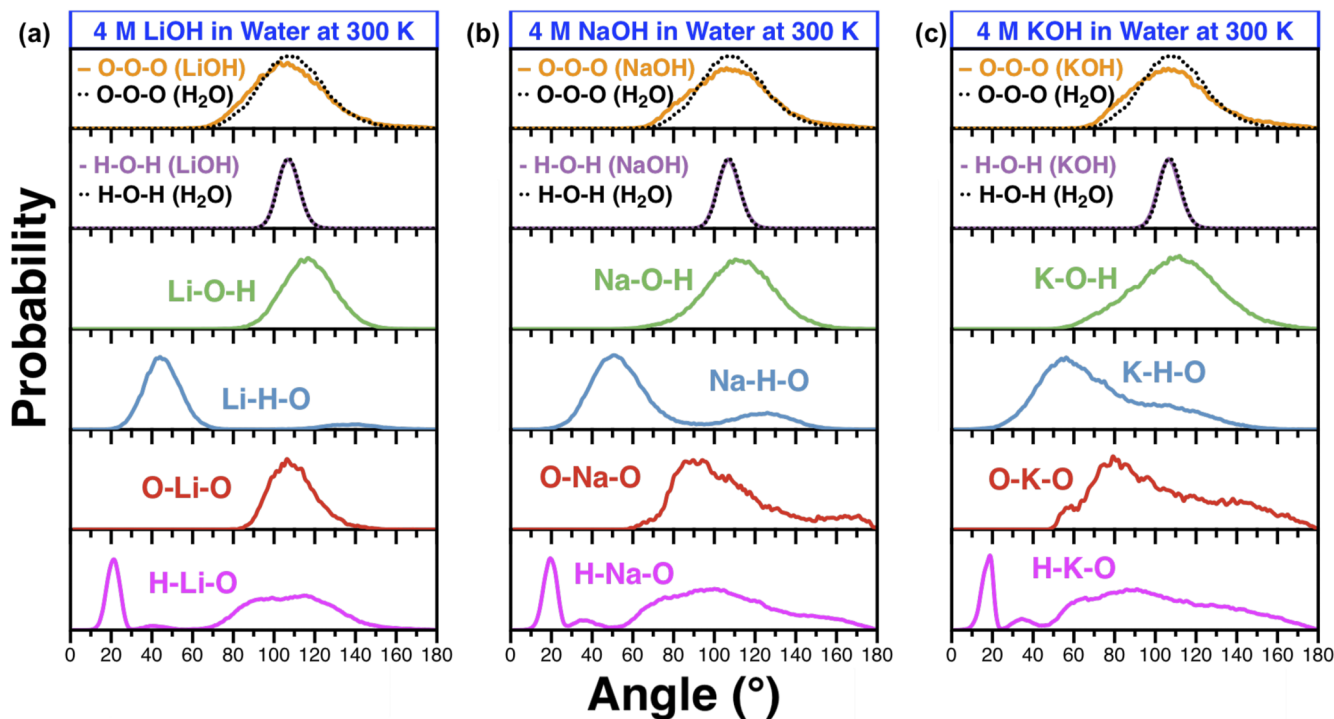


FIG. 17. Bond angle of 4M LiOH (a), NaOH (b), and KOH (c) in water solution at 300 K. The solid lines are for MOH solution ($M = \text{Li, Na, K}$), and the dotted lines are for pure water. H-M-O, magenta; O-M-O, red; M-H-O, blue; M-O-H, green; H-O-H, purple; O-O-O, orange. $M = \text{Li, Na, K}$.

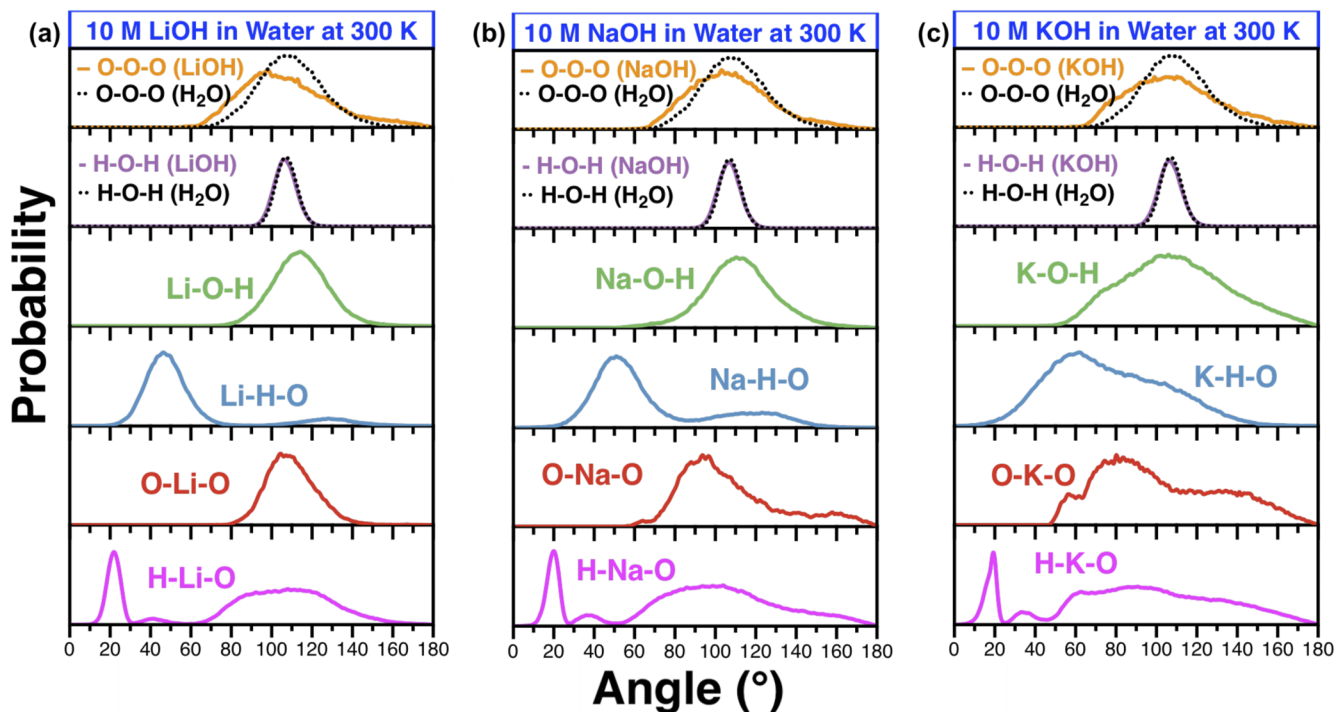


FIG. 18. Bond angle of 10M LiOH (a), NaOH (b), and KOH (c) in water solution at 300 K. The solid lines are for MOH solution ($M = \text{Li, Na, K}$), and the dotted lines are for pure water. H-M-O, magenta; O-M-O, red; M-H-O, blue; M-O-H, green; H-O-H, purple; O-O-O, orange. $M = \text{Li, Na, K}$.

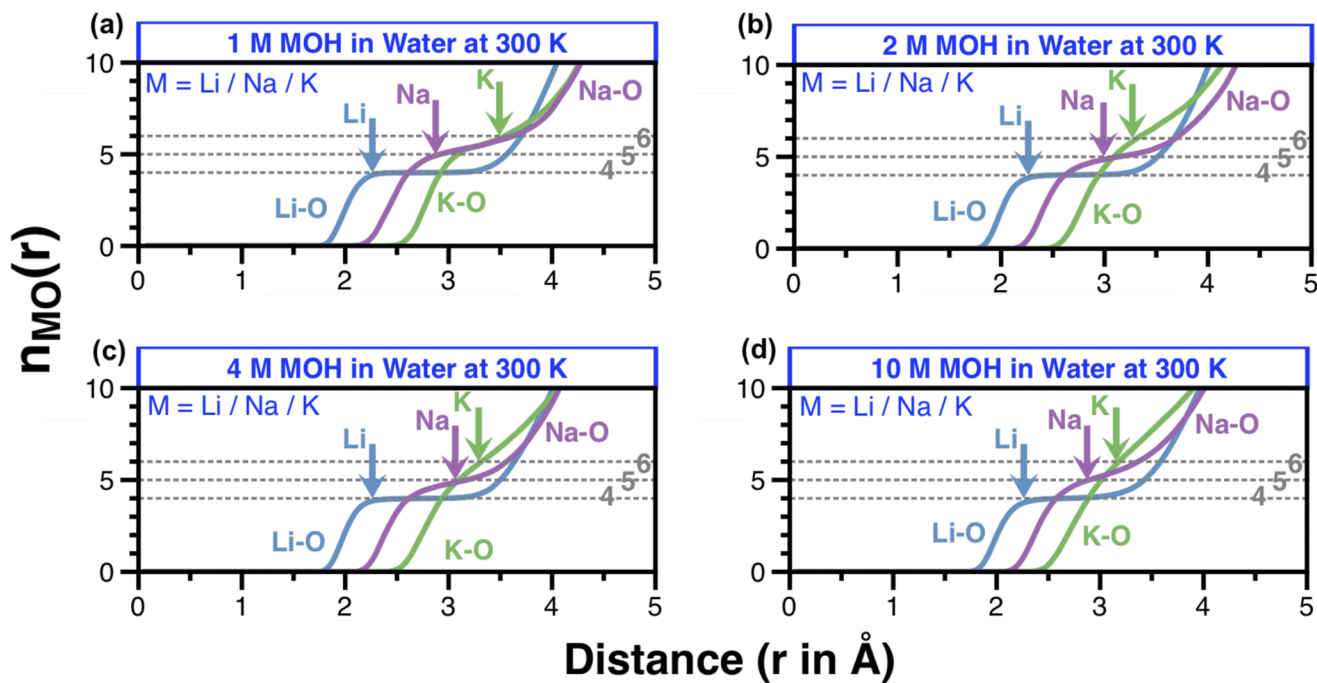


FIG. 19. M-O coordination numbers, $n(r)$, for 1M (a), 2M (b), 4M (c), and 10M (d) for MOH in water solutions at 300 K. Li-O, blue; Na-O, purple; K-O, green. The gray dashed horizontal lines signify the coordination number of 4, 5, and 6.

in KOH than in NaOH. At higher solute concentrations, 2–10M, we observe much more disordered hydration shells for NaOH and KOH. These results indicate that larger ionic radii and larger solute concentrations give rise to more disordered cation hydration shells, due to increased geometrical frustration. A similar effect of ionic radius on the structure of cationic hydration shell was observed in the dilute concentration limit using QMD simulations.⁷⁶

B. Dynamical properties

We next study vibrational correlations by computing velocity and current autocorrelation functions. The velocity autocorrelation function is defined as $F(t) = \langle \mathbf{v}_i(t) \cdot \mathbf{v}_i(0) \rangle / \langle \mathbf{v}_i(0) \cdot \mathbf{v}_i(0) \rangle$, where $\mathbf{v}_i(t)$ is the velocity of the i th atom at time t and the brackets denote the averages over ensembles and atoms. The current–current correlation function is defined as $G(t) = \langle \mathbf{J}(t) \cdot \mathbf{J}(0) \rangle / \langle \mathbf{J}(0) \cdot \mathbf{J}(0) \rangle$, where the charge current is given by $\mathbf{J}(t) = \sum_i z_i \mathbf{v}_i(t)$ with z_i being the charge of the i th ion.

The vibrational density of states is obtained by the Fourier transform of the corresponding velocity autocorrelation function,⁶¹

$$F_\alpha(\omega) = \frac{6N_\alpha}{\pi} \int_0^\infty F_\alpha(t) \cos(\omega t) dt, \quad (5)$$

where N_α is the number of atoms of species α .

The frequency-dependent ionic conductivity can be calculated from the Fourier transform of the current–current correlation function,

$$G(\omega) = \frac{2\langle J(0)^2 \rangle}{3Vk_B T} \int_0^\infty G(t) \cos(\omega t) dt, \quad (6)$$

where V is the volume of the system and k_B is the Boltzmann constant.

As a reference point, Fig. 20 shows the vibrational density of states and frequency-dependent ionic conductivity for pure water (H_2O). The blue, green, purple, and orange lines correspond to $G(\omega)$, $F_\alpha(\omega)$ of total, cation H, and anion O. The red arrows with associated numbers show peak positions from our simulation, whereas the black values are from the experimental data as a comparison.⁷⁷

To understand the vibrational spectra of aqueous solutions of alkali hydroxides (LiOH, NaOH, and KOH), we start with a discussion of vibrational spectra of water. The H_2O molecule has three main experimental frequencies: O–H symmetric stretch⁷⁸ at 453.4 meV (3657 cm^{-1}), O–H asymmetric stretch⁷⁸ at 465 meV (3756 cm^{-1}), and H–O–H bending⁷⁸ at 197.7 meV (1595 cm^{-1}). These three frequencies become bands in liquid water as shown in Fig. 20, where the components' vibrational density-of-states $F_H(\omega)$ and $F_O(\omega)$ of total $F(\omega)$ are also shown. We have also calculated the current–current auto-correlation function, and its Fourier transform is shown in the lower part of Fig. 20. Whereas the vibrational density-of-states show all vibrational modes, independent of any selection rules, $G(\omega)$ only picks dipole active modes. Since the three intramolecular modes of water are dipole active, a direct comparison with $G(\omega)$ in liquid water is of great value. In our QMD simulations of liquid water, we observe these symmetric and asymmetric O–H peaks at 406.6 and 424.6 meV and the H–O–H peak at 203 meV that clearly track the molecular frequencies of an isolated H_2O molecule.

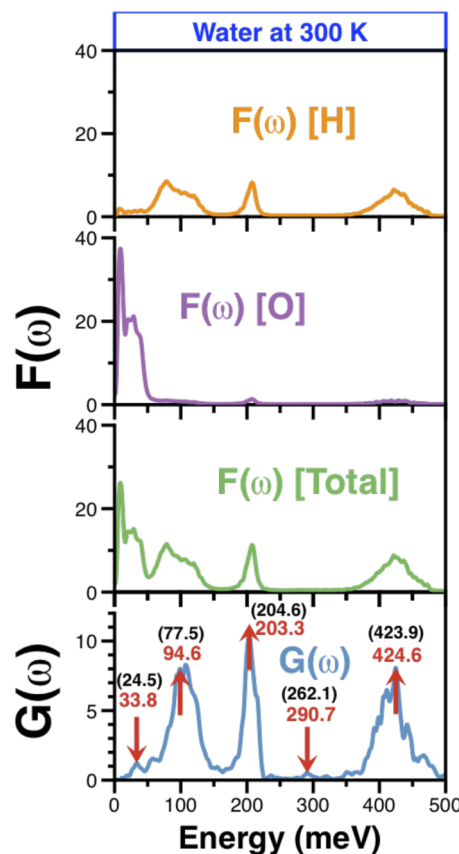


FIG. 20. Vibrational density of states $F(\omega)$ and Fourier transform of the current–current correlation $G(\omega)$ for pure water at 300 K. $G(\omega)$, blue; $F(\omega)$ (total), green; $F(\omega)$ (O), purple; $F(\omega)$ (H), orange. In the bottom figure, the peaks of $G(\omega)$ are marked by red arrows. Numbers are peak positions—the simulation values are in red and the experimental values are in black.

Our study agrees with the OH bending and stretching feature at ~ 200 and 450 meV, respectively.^{79–83} In addition to these intramolecular vibrations of H_2O molecule, in liquid water, we will have modes arising from O–O interactions between molecules and modes arising from small water clusters and a variety of rotational–translational modes. These occur in a low frequency part below 150 meV. The peak around ~ 30 meV has been attributed to the frequency of the hydrogen bond stretches.⁸⁴ The reorientation of the water molecules has been attributed to the peak at 94 meV.

It should be pointed out here that the discrepancy between our simulations and experiment is primarily due to pseudo-potential approximation and the choice of SCAN exchange–correlation function used in DFT calculations. To the best of our knowledge, no exchange–correlation function reproduces experimental frequencies in liquid water. Whereas structural correlations are determined by the location of potential energy minima, the frequencies are determined by the curvature of the potential energy function at the minima. There are infinite number of curvature values for the correct value of the minima; therefore, the deviation between the experimental and simulation values for vibrational modes in liquid

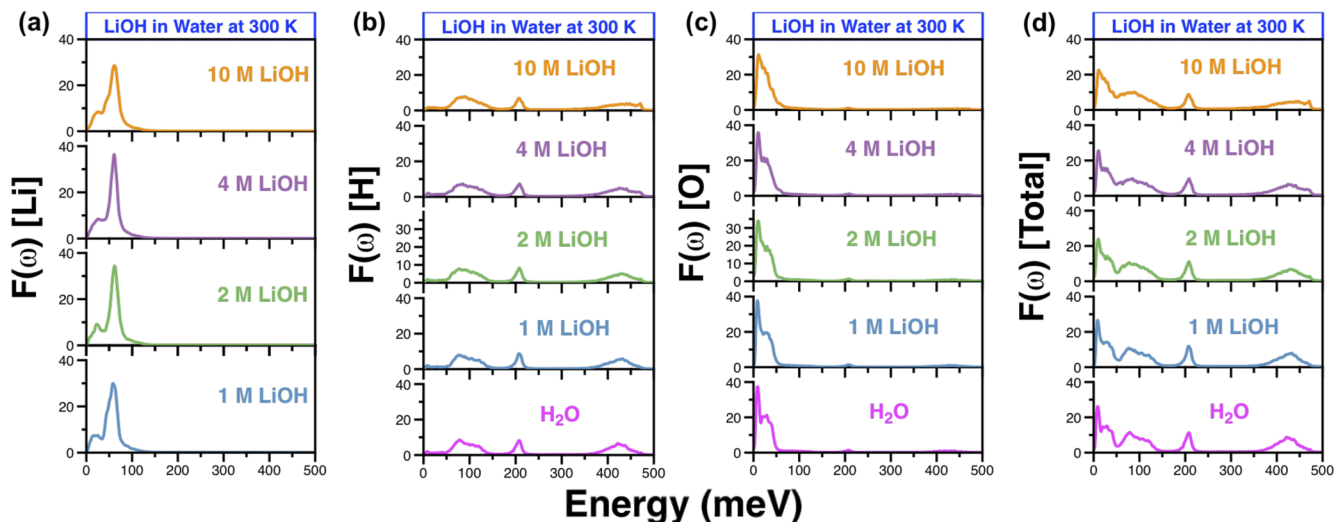


FIG. 21. Vibrational density of states of cation Li (a), H (b), anion O (c), and total (d) for LiOH in water solution at 300 K. 1M LiOH, blue; 2M LiOH, green; 4M LiOH, purple; 10M LiOH, orange.

are much more substantial when compared to structural values. However, these deviations between the simulation and experimental values in vibrational modes in liquid can be used as a tool to refine the exchange–correlation functions used in DFT calculations for water and related systems.

Since we are dealing with dilute solutions of alkali hydroxides in water, the above discussions are an easy guide to an understanding of the vibrational spectra of aqueous solutions of alkali hydroxide (LiOH, NaOH, and KOH) systems.

Figures 21–23 show the vibrational density of states of cation M, H, anion O, and total for MOH ($M \in \{\text{Li, Na, K}\}$) at 1, 2, 4, and

10M solute concentrations. The blue, green, purple, and orange lines correspond to 1, 2, 4, and 10M. The magenta lines are for pure water.

Figure 24 shows the frequency-dependent ionic conductivity for MOH ($M \in \{\text{Li, Na, K}\}$) at 1, 2, 4, and 10M solute concentrations. The blue, green, purple, and orange lines correspond to 1, 2, 4, and 10M. As a comparison, the magenta lines are for pure water.

Figures 25–28 show the vibrational density of states and frequency-dependent ionic conductivity for MOH ($M \in \{\text{Li, Na, K}\}$), respectively, at 1, 2, 4, and 10M solute concentrations. The magenta, blue, green, purple, and orange

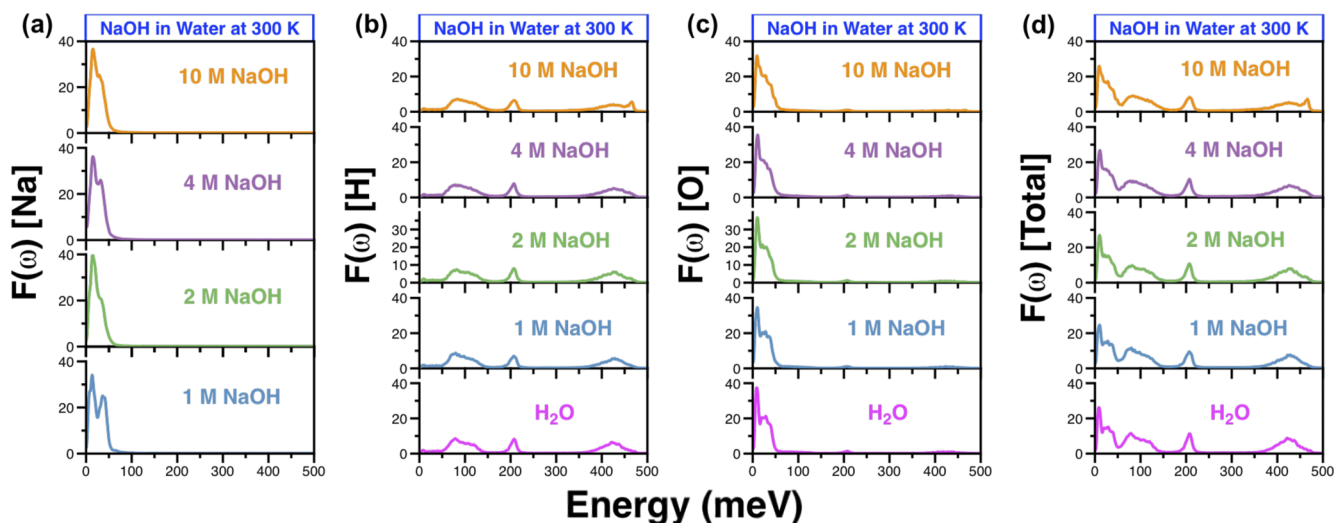


FIG. 22. Vibrational density of states of cation Na (a), H (b), anion O (c), and total (d) for NaOH in water solution at 300 K. 1M NaOH, blue; 2M NaOH, green; 4M NaOH, purple; 10M NaOH, orange.

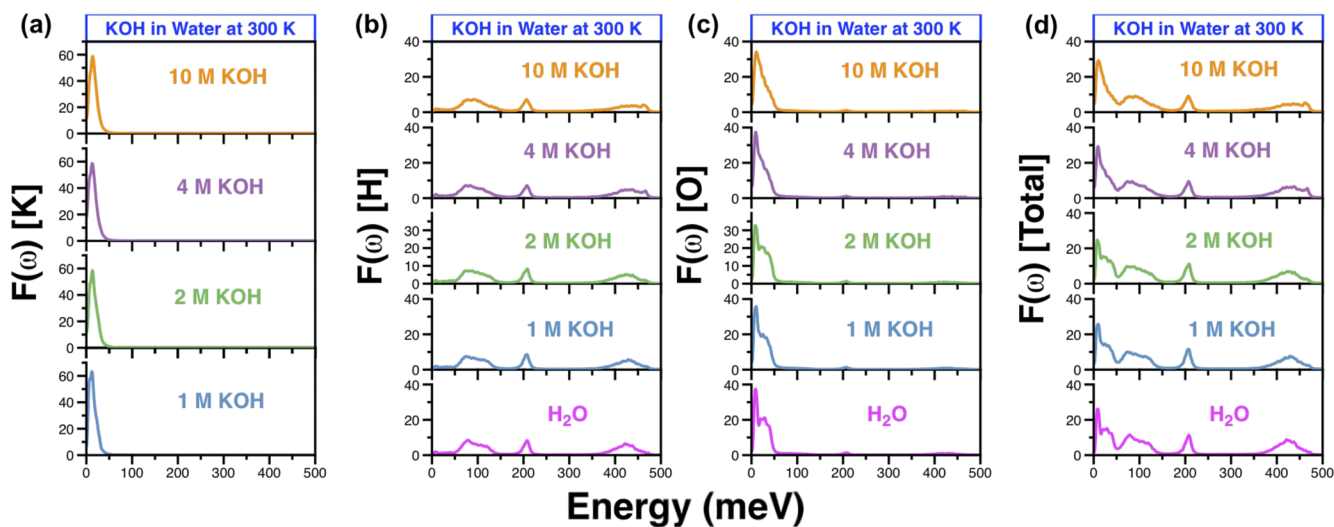


FIG. 23. Vibrational density of states of cation K (a), H (b), anion O (c), and total (d) for KOH in water solution at 300 K. 1M KOH, blue; 2M KOH, green; 4M KOH, purple; 10M KOH, orange.

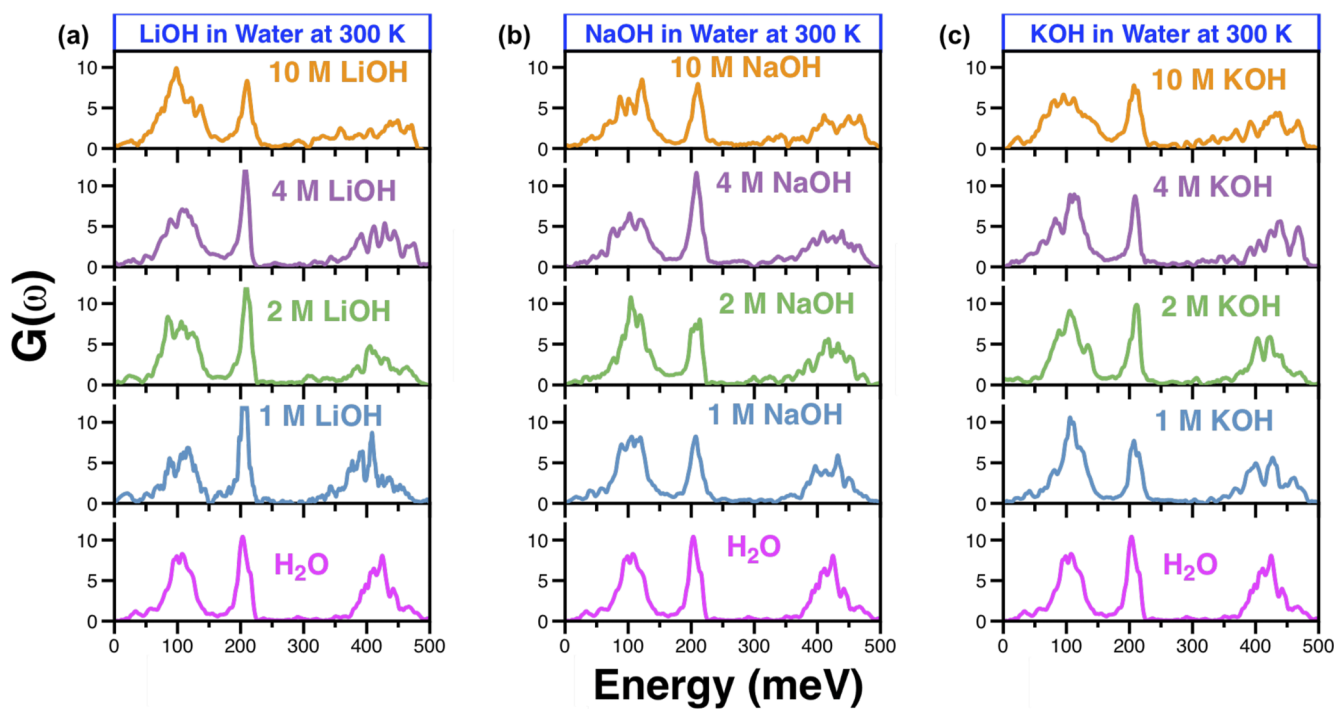


FIG. 24. Frequency-dependent ionic conductivity for LiOH (a), NaOH (b), and KOH (c) in water solution at 300 K. Pure water, magenta; 1M MOH, blue; 2M MOH, green; 4M MOH, purple; 10M MOH, orange. M = Li, Na, K.

lines correspond to $G(w)$, $F_{\alpha}(w)$ of total, cation M, H, and anion O.

From the above figures, it is easy to see that the H–O–H symmetric and antisymmetric modes in these solutions correspond

to symmetric and antisymmetric modes⁷⁸ of a single H₂O molecule at 453.4 meV and 465 meV, respectively. These modes are most strongly affected by LiOH, NaOH, and KOH in water, especially at higher concentrations.

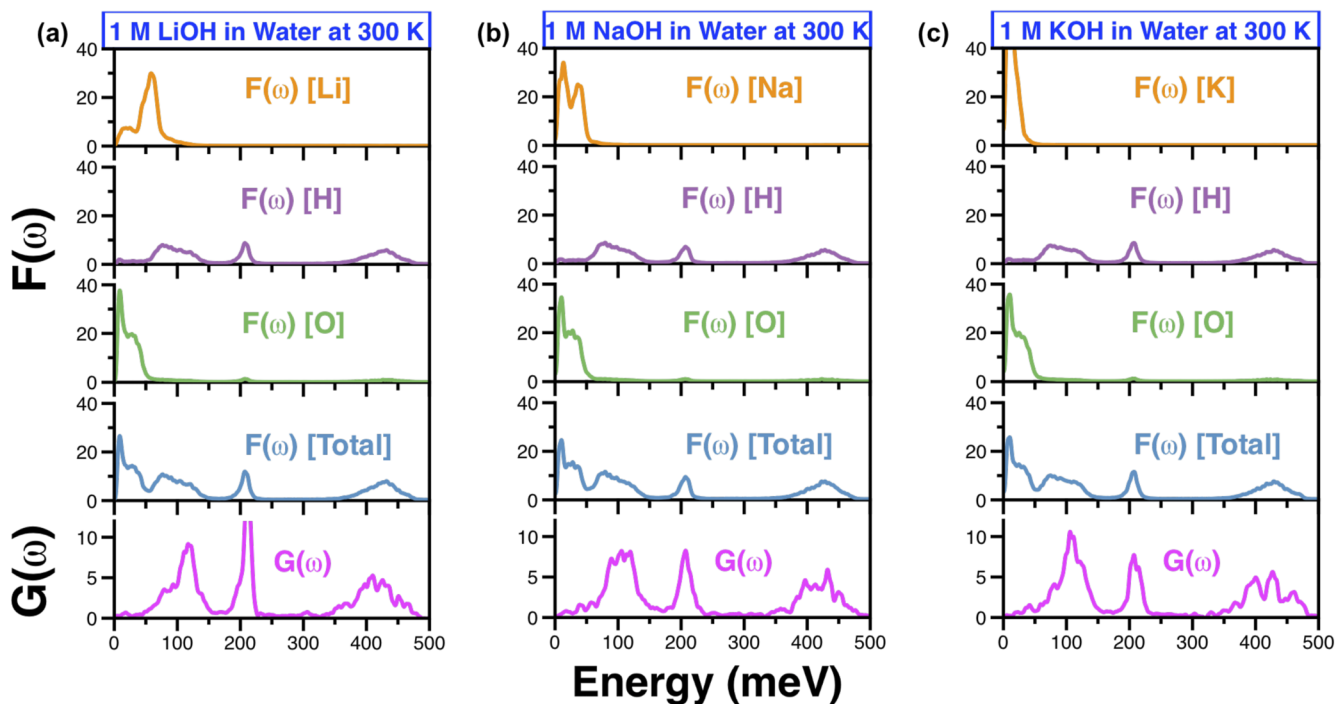


FIG. 25. Density of states $F(\omega)$ and current-current correlation $G(\omega)$ for 1M LiOH (a), NaOH (b), and KOH (c) in water solution at 300 K. $G(\omega)$, magenta; $F(\omega)$ (total), blue; $F(\omega)$ (O), green; $F(\omega)$ (H), purple; $F(\omega)$ (M), orange. M = Li, Na, K.

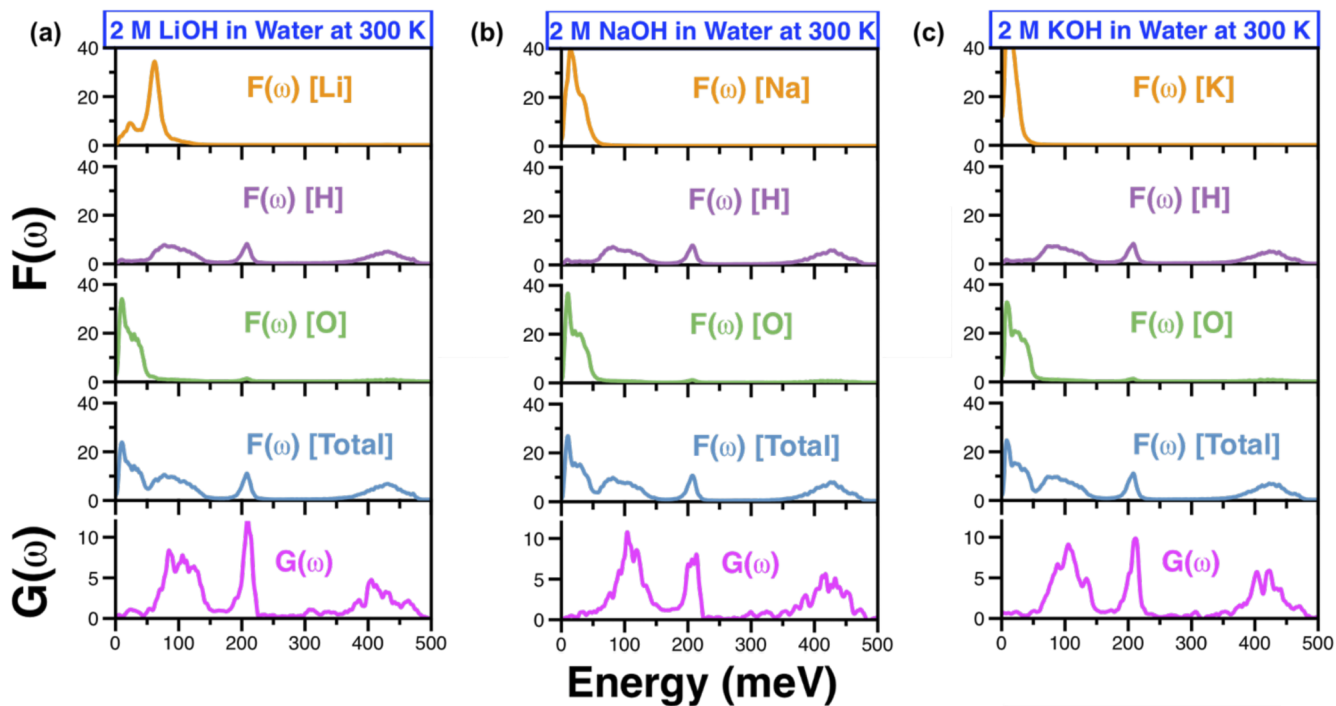


FIG. 26. Density of states $F(\omega)$ and current-current correlation $G(\omega)$ for 2M LiOH (a), NaOH (b), and KOH (c) in water solution at 300 K. $G(\omega)$, magenta; $F(\omega)$ (total), blue; $F(\omega)$ (O), green; $F(\omega)$ (H), purple; $F(\omega)$ (M), orange. M = Li, Na, K.

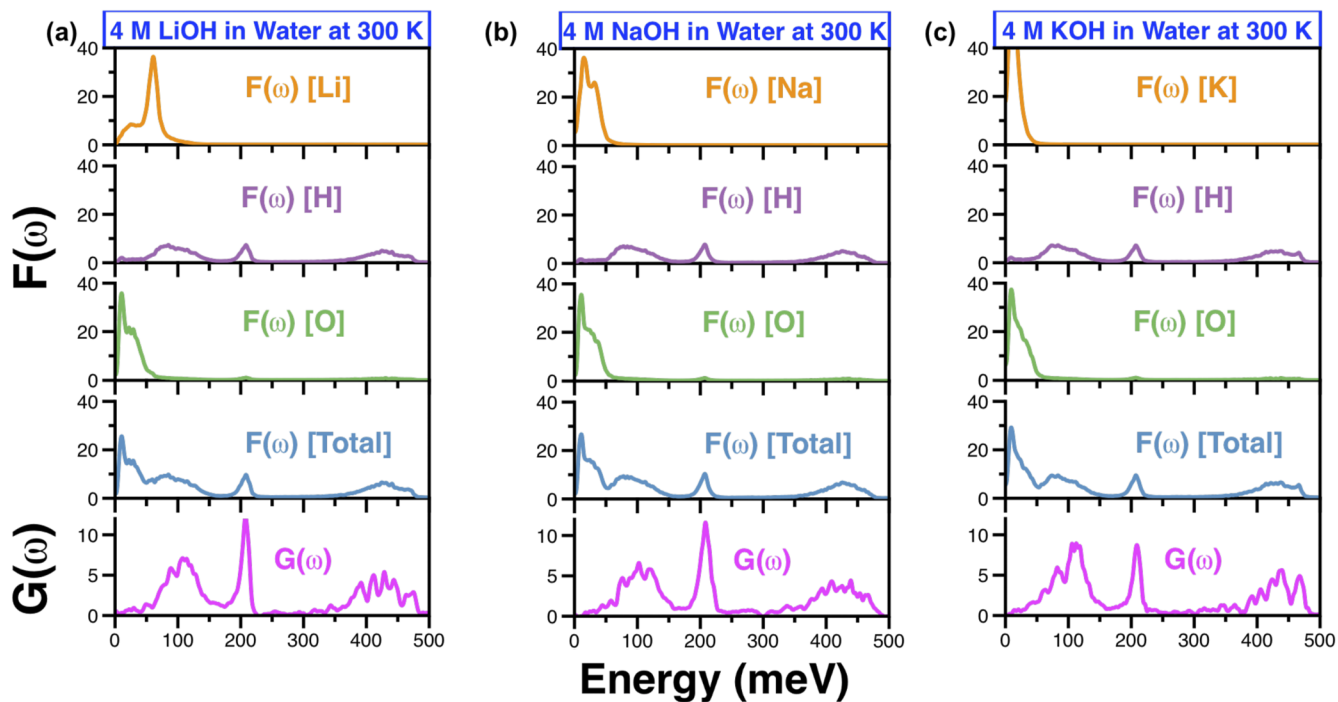


FIG. 27. Density of states $F(\omega)$ and current-current correlation $G(\omega)$ for 4M LiOH (a), NaOH (b), and KOH (c) in water solution at 300 K. $G(\omega)$, magenta; $F(\omega)$ (total), blue; $F(\omega)$ (O), green; $F(\omega)$ (H), purple; $F(\omega)$ (M), orange. M = Li, Na, K.

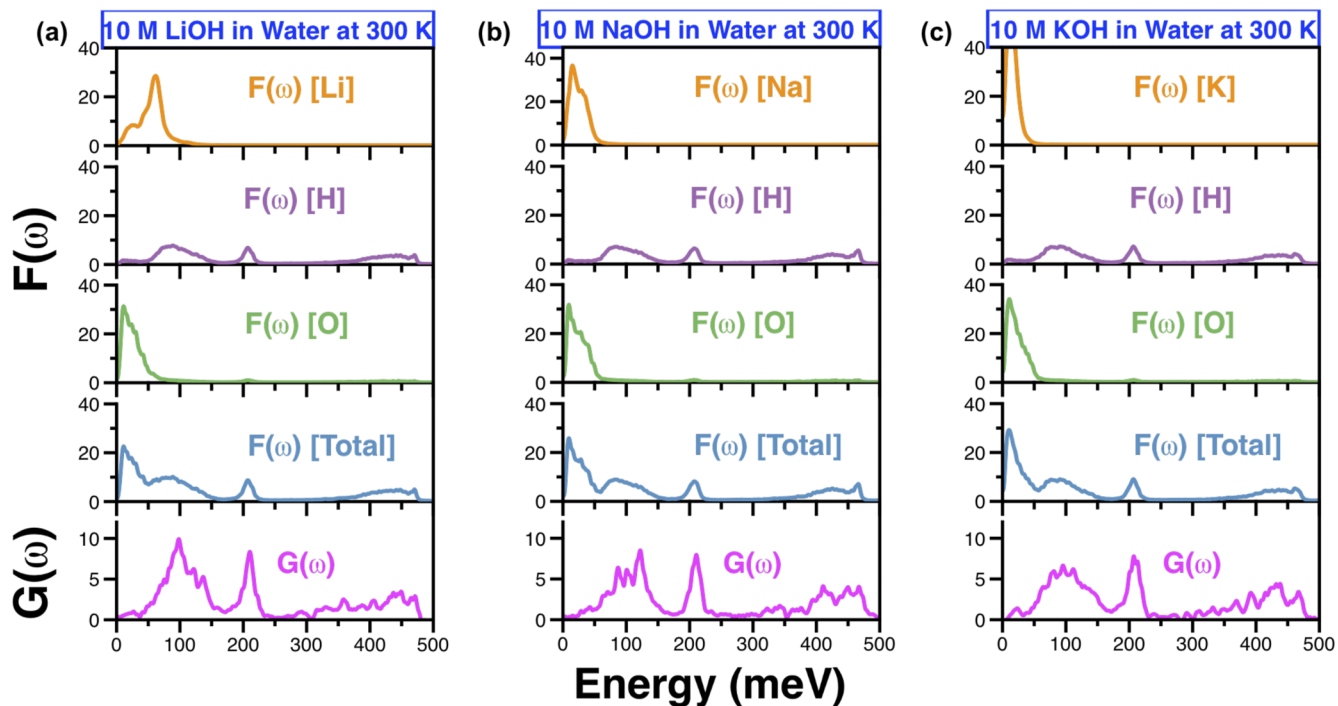


FIG. 28. Density of states $F(\omega)$ and current-current correlation $G(\omega)$ for 10M LiOH (a), NaOH (b), and KOH (c) in water solution at 300 K. $G(\omega)$, magenta; $F(\omega)$ (total), blue; $F(\omega)$ (O), green; $F(\omega)$ (H), purple; $F(\omega)$ (M), orange. M = Li, Na, K.

V. SUMMARY

We have provided comprehensive computational data for structural and vibrational properties for aqueous solutions of alkali hydroxides (LiOH, NaOH, and KOH) using quantum molecular dynamics simulations for solute concentrations ranging between 1 and 10M. Atomistic structures underlying neutron and x-ray structure factors have been studied, including positive correlations between the effects of cationic radii and solute concentrations. We have also validated the calculated structural properties with available neutron data. In addition, velocity and current autocorrelation functions have been computed, along with the corresponding vibrational spectra to be compared with inelastic neutron scattering and other optical experiments. We are currently planning neutron-scattering experiments on these systems using these *ab initio* data as a guidance.

ACKNOWLEDGMENTS

This research was supported by the U.S. Department of Energy, Office of Basic Energy Sciences, Division of Materials Sciences and Engineering, Neutron Scattering and Instrumentation Sciences program, under Award No. DE-SC0023146.

AUTHOR DECLARATIONS

Conflict of Interest

The authors have no conflicts to disclose.

Author Contributions

Ruru Ma: Formal analysis (equal); Investigation (equal); Methodology (equal); Validation (equal); Visualization (equal); Writing – original draft (equal); Writing – review & editing (equal). **Nitish Baradwaj:** Formal analysis (equal); Investigation (equal); Methodology (equal); Validation (equal); Visualization (equal); Writing – original draft (equal); Writing – review & editing (equal). **Ken-ichi Nomura:** Formal analysis (equal); Investigation (equal); Methodology (equal); Validation (equal); Visualization (equal); Writing – original draft (equal); Writing – review & editing (equal). **Aravind Krishnamoorthy:** Formal analysis (equal); Investigation (equal); Methodology (equal); Writing – review & editing (equal). **Rajiv K. Kalia:** Conceptualization (equal). **Aiichiro Nakano:** Conceptualization (equal); Formal analysis (equal); Investigation (equal); Methodology (equal); Writing – review & editing (equal). **Priya Vashishta:** Conceptualization (equal); Funding acquisition (equal); Project administration (equal); Validation (equal); Writing – review & editing (equal).

DATA AVAILABILITY

The data that support the findings of this study are available from the corresponding author upon reasonable request.

REFERENCES

¹D. Semrouni, H.-W. Wang, S. B. Clark, C. I. Pearce, K. Page, G. Schenter, D. J. Wesolowski, A. G. Stack, and A. E. Clark, *Phys. Chem. Chem. Phys.* **21**(13), 6828–6838 (2019).

- ²A. R. Hind, S. K. Bhargava, and S. C. Grocott, *Colloids Surf., A* **146**(1–3), 359–374 (1999).
- ³J. Joo, J. Kim, J. W. Kim, J. D. Ocon, J. K. Lee, W. Chang, and J. Lee, *Sep. Purif. Technol.* **145**, 24–28 (2015).
- ⁴M. Manickam, P. Singh, T. B. Issa, S. Thurgate, and R. De Marco, *J. Power Sources* **130**(1–2), 254–259 (2004).
- ⁵S. Stolbov and T. S. Rahman, *arXiv:cond-mat/0407404* (2004).
- ⁶T. Rahman, S. Stolbov, and F. Mehmood, *Appl. Phys. A* **87**, 367–374 (2007).
- ⁷*CRC Handbook of Chemistry and Physics*, edited by J. Rumble (2017).
- ⁸J. Nagle and H. Scott, Jr., *Biochim. Biophys. Acta* **513**(2), 236–243 (1978).
- ⁹J. W. Nichols and D. W. Deamer, *Proc. Natl. Acad. Sci. U. S. A.* **77**(4), 2038–2042 (1980).
- ¹⁰S. Paula, A. Volkov, A. Van Hoek, T. Haines, and D. W. Deamer, *Biophys. J.* **70**(1), 339–348 (1996).
- ¹¹T. H. Haines, *Prog. Lipid Res.* **40**(4), 299–324 (2001).
- ¹²D. Zahn and J. Brickmann, *Phys. Chem. Chem. Phys.* **3**(5), 848–852 (2001).
- ¹³K. Pounot, M. Appel, C. Beck, M. Weik, G. Schirò, Y. Fichou, T. Seydel, and F. Schreiber, *JoVE* **182**, e63664 (2022).
- ¹⁴I. Restrepo-Angulo, A. De Vizcaya-Ruiz, and J. Camacho, *J. Appl. Toxicol.* **30**(6), 497–512 (2010).
- ¹⁵N. N. Greenwood and A. Earnshaw, *Chemistry of the Elements* (Elsevier, 2012).
- ¹⁶J.-M. Tarascon and M. Armand, *Nature* **414**(6861), 359–367 (2001).
- ¹⁷W. H. Bauer, A. P. Finkelstein, and S. E. Wiberley, *ASLE Trans.* **3**(2), 215–224 (1960).
- ¹⁸A. Razmjou, M. Asadnia, E. Hosseini, A. Habibnejad Korayem, and V. Chen, *Nat. Commun.* **10**(1), 5793 (2019).
- ¹⁹J. Xiao, B. Niu, and Z. Xu, *J. Hazard. Mater.* **418**, 126319 (2021).
- ²⁰J. Xiao, J. Li, and Z. Xu, *Environ. Sci. Technol.* **54**(1), 9–25 (2019).
- ²¹J. Xiao, B. Niu, Q. Song, L. Zhan, and Z. Xu, *J. Hazard. Mater.* **404**, 123947 (2021).
- ²²J. Xiao, R. Gao, B. Niu, and Z. Xu, *J. Hazard. Mater.* **407**, 124704 (2021).
- ²³X. Wei, W. Gao, Y. Wang, K. Wu, and T. Xu, *Sep. Purif. Technol.* **280**, 119909 (2022).
- ²⁴S. Ansell and G. Neilson, *J. Chem. Phys.* **112**(9), 3942–3944 (2000).
- ²⁵F. Bruni, M. A. Ricci, and A. K. Soper, *J. Chem. Phys.* **114**(18), 8056–8063 (2001).
- ²⁶H.-K. Nienhuys, A. J. Lock, R. A. van Santen, and H. J. Bakker, *J. Chem. Phys.* **117**(17), 8021–8029 (2002).
- ²⁷A. W. Omta, M. F. Kropman, S. Woutersen, and H. J. Bakker, *Science* **301**(5631), 347–349 (2003).
- ²⁸A. Filipponi, S. De Panfilis, C. Oliva, M. A. Ricci, P. D’Angelo, and D. T. Bowron, *Phys. Rev. Lett.* **91**(16), 165505 (2003).
- ²⁹A. Botti, F. Bruni, S. Imberti, M. A. Ricci, and A. K. Soper, *J. Chem. Phys.* **119**(10), 5001–5004 (2003).
- ³⁰A. Botti, F. Bruni, S. Imberti, M. A. Ricci, and A. K. Soper, *J. Chem. Phys.* **120**(21), 10154–10162 (2004).
- ³¹A. Botti, F. Bruni, S. Imberti, M. Ricci, and A. Soper, *J. Chem. Phys.* **121**(16), 7840–7848 (2004).
- ³²P. Gehring, M. Helgeson, D. Louca, B. Olsen, K. A. Ross, N. Ross, C. Saunders, and Y. Xi, *Neutron News* **32**(1), 2–6 (2021).
- ³³J. Tomkinson, C. Carlile, S. Lovesey, R. Osborn, and A. Taylor, *Adv. Spectrosc.* **19**, 135–214 (1991).
- ³⁴J. A. White, E. Schwegler, G. Galli, and F. Gygi, *J. Chem. Phys.* **113**(11), 4668–4673 (2000).
- ³⁵M. E. Tuckerman, D. Marx, and M. Parrinello, *Nature* **417**(6892), 925–929 (2002).
- ³⁶D. Marx, M. E. Tuckerman, and M. Parrinello, *J. Phys.: Condens. Matter* **12**(8A), A153 (2000).
- ³⁷Z. Zhu and M. E. Tuckerman, *J. Phys. Chem. B* **106**(33), 8009–8018 (2002).
- ³⁸B. Chen, J. M. Park, I. Ivanov, G. Tabacchi, M. L. Klein, and M. Parrinello, *J. Am. Chem. Soc.* **124**(29), 8534–8535 (2002).
- ³⁹B. Chen, I. Ivanov, J. M. Park, M. Parrinello, and M. L. Klein, *J. Phys. Chem. B* **106**(46), 12006–12016 (2002).

- ⁴⁰D. Asthagiri, L. R. Pratt, J. D. Kress, and M. A. Gomez, *Proc. Natl. Acad. Sci. U. S. A.* **101**(19), 7229–7233 (2004).
- ⁴¹D. Asthagiri, L. R. Pratt, J. Kress, and M. Gomez, *Chem. Phys. Lett.* **380**(5–6), 530–535 (2003).
- ⁴²A. Lyubartsev, K. Laasonen, and A. d. Laaksonen, *J. Chem. Phys.* **114**(7), 3120–3126 (2001).
- ⁴³H. H. Loeffler and B. M. Rode, *J. Chem. Phys.* **117**(1), 110–117 (2002).
- ⁴⁴T. Qin, R. M. Wentzcovitch, K. Umamoto, M. M. Hirschmann, and D. L. Kohlstedt, *Am. Mineral.* **103**(5), 692–699 (2018).
- ⁴⁵B. Prével, J. Jal, J. Dupuy-Philon, and A. Soper, *J. Chem. Phys.* **103**(5), 1886–1896 (1995).
- ⁴⁶B. Prevel, J. Jal, J. Dupuy-Philon, and A. Soper, *J. Chem. Phys.* **103**(5), 1897–1903 (1995).
- ⁴⁷B. Prevel, J. Jal, J. Dupuy-Philon, and A. Soper, *Physica A* **201**(1–3), 312–317 (1993).
- ⁴⁸T. Yamaguchi, H. Ohzono, M. Yamagami, K. Yamanaka, K. Yoshida, and H. Wakita, *J. Mol. Liq.* **153**(1), 2–8 (2010).
- ⁴⁹R. Tromp, G. Neilson, and A. Soper, *J. Chem. Phys.* **96**(11), 8460–8469 (1992).
- ⁵⁰R. Beudert, H. Bertagnolli, and M. Zeller, *J. Chem. Phys.* **106**(21), 8841–8848 (1997).
- ⁵¹M. Cabaço, A. Gaspar, C. M. d. Morais, and M. A. Marques, *J. Phys.: Condens. Matter* **12**(12), 2623 (2000).
- ⁵²N. Skipper and G. Neilson, *J. Phys.: Condens. Matter* **1**(26), 4141 (1989).
- ⁵³S. Imberti, A. Botti, F. Bruni, G. Cappa, M. A. Ricci, and A. K. Soper, *J. Chem. Phys.* **122**(19), 194509 (2005).
- ⁵⁴D. J. Morris, K. Siemensmeyer, J.-U. Hoffmann, I. Glavatskyi, B. Klemke, D. Tennant, S. Isakov, and R. Moessner, presented at the APS March Meeting Abstracts, 2018.
- ⁵⁵G. W. Brady and J. T. Krause, *J. Chem. Phys.* **27**(1), 304–308 (1957).
- ⁵⁶T. Megyes, S. Bálint, T. Grósz, T. Radnai, I. Bakó, and P. Sipos, *J. Chem. Phys.* **128**(4), 044501 (2008).
- ⁵⁷C. Chen, C. Huang, I. Waluyo, D. Nordlund, T.-C. Weng, D. Sokaras, T. Weiss, U. Bergmann, L. G. M. Pettersson, and A. Nilsson, *J. Chem. Phys.* **138**(15), 154506 (2013).
- ⁵⁸M. Zapałowski and W. M. Bartczak, *Comput. Chem.* **24**(3–4), 459–468 (2000).
- ⁵⁹M. Hellström and J. Behler, *Phys. Chem. Chem. Phys.* **19**(1), 82–96 (2017).
- ⁶⁰J. Sun, A. Ruzsinszky, and J. P. Perdew, *Phys. Rev. Lett.* **115**(3), 036402 (2015).
- ⁶¹A. Krishnamoorthy, K. Nomura, N. Baradwaj, K. Shimamura, P. Rajak, A. Mishra, S. Fukushima, F. Shimojo, R. Kalia, A. Nakano, and P. Vashishta, *Phys. Rev. Lett.* **126**(21), 216403 (2021).
- ⁶²G. Kresse and J. Furthmüller, *Phys. Rev. B* **54**(16), 11169–11186 (1996).
- ⁶³M. C. Payne, M. P. Teter, D. C. Allan, T. A. Arias, and J. D. Joannopoulos, *Rev. Mod. Phys.* **64**(4), 1045–1097 (1992).
- ⁶⁴P. E. Blochl, *Phys. Rev. B* **50**(24), 17953–17979 (1994).
- ⁶⁵P. Hohenberg and W. Kohn, *Phys. Rev.* **136**(3B), B864–B871 (1964).
- ⁶⁶P. Vashishta, R. K. Kalia, J. P. Rino, and I. Ebbsjo, *Phys. Rev. B* **41**(17), 12197–12209 (1990).
- ⁶⁷A. K. Soper and E. R. Barney, *J. Appl. Crystallogr.* **44**(4), 714–726 (2011).
- ⁶⁸A. K. Soper, *Mol. Phys.* **107**(16), 1667–1684 (2009).
- ⁶⁹M. Ernzerhof and G. E. Scuseria, *J. Chem. Phys.* **110**(11), 5029–5036 (1999).
- ⁷⁰V. S. Bryantsev, M. S. Diallo, A. C. T. van Duin, and W. A. Goddard III, *J. Chem. Theory Comput.* **5**(4), 1016–1026 (2009).
- ⁷¹R. P. Feynman, A. R. Hibbs, and D. F. Styer, *Quantum Mechanics and Path Integrals* (Courier Corporation, 2010).
- ⁷²J. Cao and G. A. Voth, *J. Chem. Phys.* **101**(7), 6168–6183 (1994).
- ⁷³S. Habershon, D. E. Manolopoulos, T. E. Markland, and T. F. Miller III, *Annu. Rev. Phys. Chem.* **64**, 387–413 (2013).
- ⁷⁴A. K. T. M. Linker, L. L. Daemen, A. J. Ramirez-Cuesta, K. Nomura, A. Nakano, Y. Q. Cheng, W. R. Hicks, A. I. Kolesnikov, and P. D. Vashishta, “Neutron scattering and neural-network quantum molecular dynamics investigation of the vibrations of ammonia along the solid-to-liquid transition,” *Nature Commun.* (to be published).
- ⁷⁵A. Musaelian, S. Batzner, A. Johansson, L. Sun, C. J. Owen, M. Kornbluth, and B. Kozinsky, *Nat. Commun.* **14**(1), 579 (2023).
- ⁷⁶T. Ikeda, M. Boero, and K. Terakura, *J. Chem. Phys.* **126**(3), 034501 (2007).
- ⁷⁷G. R. Medders and F. Paesani, *J. Chem. Theory Comput.* **11**(3), 1145–1154 (2015).
- ⁷⁸K. Nakamoto, *Infrared and Raman Spectra of Inorganic and Coordination Compounds, Part B: Applications in Coordination, Organometallic, and Bioinorganic Chemistry* (John Wiley & Sons, 2009).
- ⁷⁹G. S. Fanourgakis and S. S. Xantheas, *J. Chem. Phys.* **128**(7), 074506 (2008).
- ⁸⁰C. Burnham, D. Anick, P. Mankoo, and G. Reiter, *J. Chem. Phys.* **128**(15), 154519 (2008).
- ⁸¹P. K. Mankoo and T. Keyes, *J. Chem. Phys.* **129**(3), 034504 (2008).
- ⁸²T. Ishiyama and A. Morita, *J. Chem. Phys.* **131**(24), 244714 (2009).
- ⁸³T. Hasegawa and Y. Tanimura, *J. Phys. Chem. B* **115**(18), 5545–5553 (2011).
- ⁸⁴J. E. Bertie and Z. Lan, *Appl. Spectrosc.* **50**(8), 1047–1057 (1996).